TECHNISCHE UNIVERSITÄT WIEN

INSTITUTE FOR THEORETICAL PHYSICS

DIPLOMARBEIT

Maximum information states for nanoparticles: Optimising wavefronts for precision measurements

zur Erlangung des akademischen Grades

Diplom-Ingenieur

im Rahmen des Studiums

Technische Physik

eingereicht von

Luca Neubacher

Matrikelnummer 11827175

ausgeführt am Institut für Theoretische Physik
der Fakultät für Physik der Technischen Universität Wien

Betreuung
Betreuer: Univ.Prof. Dipl.-Ing. Dr.techn. Stefan Rotter
Mitwirkung: Univ.Ass. Dipl.-Ing. Maximilian Weimar, BSc

Wien, 21.5.2025

Luca Neubacher

Stefan Rotter

Abstract

Precise measurements of physical parameters through optical scattering is fundamental to various scientific and technological applications. In this thesis, we investigate the optimisation of incident wavefronts to enhance information retrieval from scattered fields. Using Fisher information as a metric, we develop a computational framework to determine Maximum Information States (MIS) for specific scattering setups. Using generalised Lorenz-Mie theory and the T-matrix method, we simulate light scattering from different target geometries and analyse the information content captured by a camera. An optimisation algorithm is used to tailor the spatial distribution of incident beams, maximising measurement precision while adhering to experimental constraints. The methodology is applied to spherical and cylindrical scatterers, demonstrating substantial improvements over conventional beams. These findings contribute to the advancement of precision optical measurements and wavefront shaping techniques.

Contents

1 Introduction

All measurements inevitably include some degree of noise, making it impossible to measure any physical quantity with absolute certainty. Depending on the physical observable someone wants to measure, there are many different types of measurements. A popular choice is to use light or other kinds of electromagnetic radiation. Coherent light allows for precise and accurate measurements and is widely used in various physical scenarios, such as interferometry [1], holography [2], laser Doppler velocimetry [3], etc. Here, we will focus on coherent imaging of the scattered field of a small object, allowing us to extract information about a parameter of the object, such as its position or angular orientation, by measuring the object's scattered field captured by a camera.

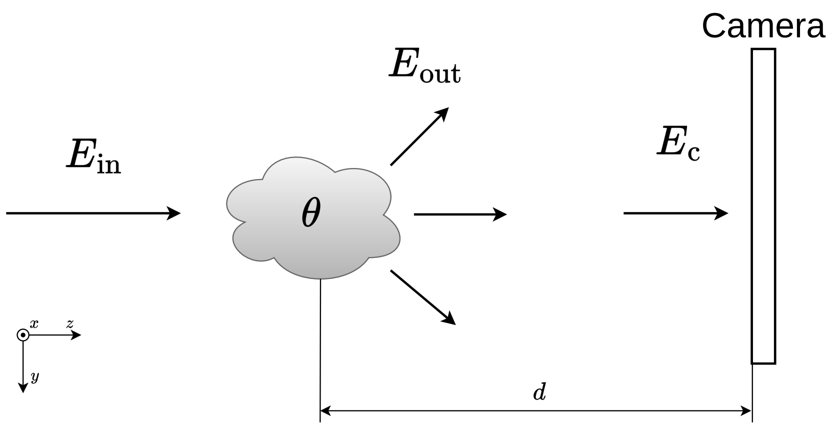

Figure 1.1: **Side view illustration of the setup.** An incoming field E_{in} scatters off an object, characterized by an unknown parameter θ (e.g., position, orientation,...). The outgoing (scattered) field E_{out} carries information on the parameter θ and propagates towards a camera. A part of this field E_{out} ends up on the camera E_{c} and generates an intensity distribution there.

Figure 1.1 shows a sketch of the setup and visualises the basic idea from such an optical imaging measurement. The incoming beam coming from the left side scatters on a target and then hits the camera on the right side. In order to improve the precision achieved by such a measurement, there are a few experimental parameters that can be tuned. The easiest change would be the type and size of camera, which tends to be expensive and results only in a slight improvement, because the resolution is limited by the coherence properties and not by the pixels. Another way to improve the precision of the measurement is to increase the intensity of the incoming beam. However, increasing the intensity results in an increased interaction with the scatterer resulting in unwanted effects, such as thermal heating and possibly even destroying the object. In this work, we take the approach of increasing the precision of the measurement by tailoring the spatial distribution of the incoming light pattern. This procedure is referred to as wavefront shaping [4].

Popular choices for the spatial distribution of an incoming beam for optical imaging include Gaussian beams, Bessel beams or Laguerre-Gaussian beams, just to name a few. Those beams might allow for a very precise measurement, but recent works [5, 6, 7] have shown that with an optimised spatial distribution of the incoming beam, it is possible to achieve even higher precision.

But what makes an incoming beam optimal to measure a parameter of our system? A powerful tool to quantify the information about this parameter, contained within the scattered field is the Fisher information and the associated Cramér-Rao lower bound. The Cramér-Rao lower bound connects the Fisher information and the best possible measurement precision, i.e., the lowest possible variance of a statistical estimator of the parameter of interest. It is possible to find and construct such an optimised spatial distribution by maximising the Fisher information[5, 6].

In [5], the authors used a homodyne detection scheme and measured the scattering matrices and derivatives of the scattering matrices by measuring the outgoing fields. This allowed them to construct a hermitian Fisher information operator. An optimal incoming spatial distribution could be designed by taking the eigenstate with the largest eigenvalue, called the maximum information state (MIS).

Using a similar approach, we develop a method to construct incoming beams with optimised spatial distribution. A striking difference to the technique mentioned above is, however, that using a camera we can only use the intensity and have no information on the phase of the field. As a result, we cannot employ the Fisher information operator to construct a maximum information state, because this would yield state with information that is inaccessible. Instead, we solve the scattering problem, simulate the corresponding camera image, and compute the associated Fisher information.

The particles we are interested in are nanoparticles, which makes the measurement particularly challenging and interesting. In order to calculate the scattering for such a target, we use the generalised Lorenz-Mie theory (GLMT). The commonly used theories for scattering (e.g., geometric optics, rayleigh approximation, etc.) cannot be used because the size of the target is in the same order as the wavelength. With the GLMT it is possible to represent any incoming beam, then calculate the scattering for spherical targets of arbitrary size.

With the inclusion of the T-matrix method it is possible to calculate the scattering for targets of generic shape. With that we can simulate the intensity distribution on a camera, which allows us to calculate the Fisher information from the camera image. This calculation enables us to use an optimisation method and find an optimal spatial distribution for the incoming beam by maximising the Fisher information arriving at the camera.

We simulate various different experimental setups and explore MIS for each of them. We investigate in particular the dependence of Fisher information on the size of the target and the connection to resonance phenomena, the so-called Mie resonances.

2 Background theory

This chapter provides a general overview of the methods used in this work. Our task requires a method for simulating the scattering of electromagnetic waves from objects that take on different shapes and different sizes comparable to the wavelength. For that sake we make use of the so-called generalised Lorenz-Mie theory. Lorenz-Mie theory, which was independently developed by Lorenz [8] and Mie [9] allowed for the calculation of a plane wave scattered by a homogeneous sphere. Later, this theory was generalised to represent any kind of incoming beams. Calculating the scattering of a non-spherical particle can be done with the T-matrix method originally formulated by Waterman [10, 11], which is closely related to the generalised Lorenz-Mie theory.

With a theory in place, which is capable of solving our scattering problem, we can calculate the camera images for every experimental setup that we consider. What we need now is a way to judge how precisely we can measure a parameter for a given beam. For that sake, we introduce the quantity of Fisher information and the corresponding Cramér-Rao lower bound. With both of them, we can make a statement about the performance of the beam, as will be explained in a later section. Furthermore, we can use Fisher information as a cost function in the optimisation process searching for a beam that extracts the maximum amount of Fisher information about the parameter of interest.

2.1 Generalised Lorenz-Mie theory

Before we can calculate the camera image of a scattering object illuminated by coherent light and the corresponding Fisher information about the desired parameter that arrives on the camera screen, we need a way of calculating the fields after the scattering. We can then use this method to get the intensity distribution on the camera, which we need for quantifying the Fisher information that arrives on the camera.

Simple models such as the Rayleigh approximation and geometric optics are not capable of calculating the scattered fields if the size of the scatterer is of the same order as the wavelength. A solution to this problem comes with generalised Lorenz-Mie theory (GLMT), whereby a multipole expansion is used to describe the scattering of electromagnetic waves.

With the GLMT, it is possible to solve complex scattering problems for spherical particles of any size. For non-spherical particles, this theory can be extended to the so-called

T-matrix method (see 2.1.2). The GLMT uses a series of vector spherical wavefunctions (VSWFs), which are eigensolutions of the vector Helmholtz equation and form a complete orthonormal basis. With those VSWFs the electric field $\mathbf{E}$ can be described as

$$\mathbf{E}(\mathbf{r}) = \sum_{n=1}^{\infty} \sum_{m=-n}^{n} a_{nm}\mathbf{M}_{nm}(kr) + b_{nm}\mathbf{N}_{nm}(kr), \tag{2.1}$$

where $\mathbf{N}, \mathbf{M}$ are the VSWFs, a, b are the beam shape coefficients (BSCs) and $k = 2\pi/\lambda$ the wavenumber [12]. The magnetic field can be calculated in a similar way. The VSWF $\mathbf{N}$ corresponds to the TE modes of the field and the VSWF $\mathbf{M}$ to the TM modes. A more detailed description of the VSWF is in appendix A.

With that expansion, we can describe an incoming, an internal, and a scattered field. The incoming field describes the type and shape of the beam without any scattering. With a target, the fields inside (internal field) and outside (scattered field) of the target will change and are described by different BSCs. Solving the scattering problem requires to find a relation between the BSCs of the incoming field and the scattered field. The description and calculation are given in sec. 2.1.2.

A particularly important property of the beam is its power. Constraining the power is necessary to avoid a divergence in our optimisation process since increasing the power trivially increases the Fisher information content of the scattered field. A more detailed discussion will follow in section 2.2.2. Representing the beam in terms of BSCs allows to express the power of the beam by the simple expression

$$P(a, b) \propto \sum_{n=1}^{\infty} \sum_{n=-m}^{m} |a_{nm}|^2 + |b_{nm}|^2. \tag{2.2}$$

2.1.1 Beam shape coefficients and approximation

In order to characterise a beam using the VSWF-basis, it is necessary to compute the corresponding BSCs. The calculation can be done with surface integrals [13], which are given by

$$a_{nm} = \mathrm{i}\frac{\oint \mathbf{E} \cdot \mathbf{M}^*_{nm} \mathrm{d}S}{\oint |\mathbf{M}^*_{nm}|^2 \mathrm{d}S}, \qquad b_{nm} = \mathrm{i}\frac{\oint \mathbf{E} \cdot \mathbf{N}^*_{nm} \mathrm{d}S}{\oint |\mathbf{N}^*_{nm}|^2 \mathrm{d}S}. \tag{2.3}$$

For the simple case of a plane wave, the solutions of those integrals are given by

$$a_{nm} = 4\pi \mathrm{i}^n N_n \mathbf{C}^*_{nm}\mathbf{E}_0, \qquad b_{nm} = 4\pi \mathrm{i}^{n-1} N_n \mathbf{B}^*_{nm}\mathbf{E}_0. \tag{2.4}$$

Solving those integrals and finding the expansion for more complex field (e.g., Bessel beam, Gaussian beam, etc.) has been done in [14] and [15]. In [14] they derived the expansion for a Bessel beam and a Gaussian beam. In [15], they present an efficient method for determining the multipole representation of an arbitrary focused beam.

The sums in eqs. (2.1) and (2.2) over infinite terms in general cannot be calculated, and therefore the sum is truncated at a cut-off value $n_{\max}$. Taking into account that the higher order VSWFs do not contribute much around the origin instead are responsible for the field further away, it is possible to calculate a field, which converges within a given volume in a finite number of $n_{\max}$.

There are many different ways to determine the truncation number $n_{\max}$. Most of them are based on empirical observations. In [15] they used

$$n_{\max} = kr_{\text{roi}} + 3(kr_{\text{roi}})^{1/3}, \tag{2.5}$$

and in [16] they used

$$n_{\max} = kr_{\text{roi}} + 4.05(kr_{\text{roi}})^{1/3} + 2, \tag{2.6}$$

with r_{roi} being the radius of the region of interest. Both are valid options and in the end, it is always a trade-off between accuracy and computational time.

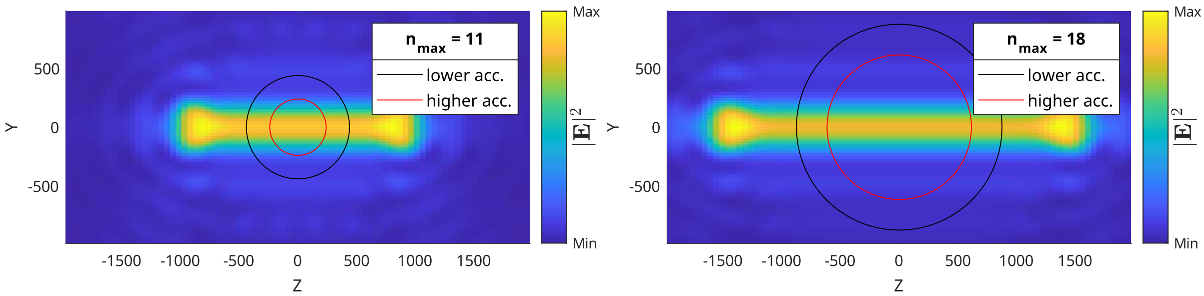

Figure 2.1: **Beam representations with different numbers of modes.** The left figure depicts a cross section of a Bessel beam of zeroth order with $n_{max} = 11$ and the right figure a cross section of the same Bessel beam with $n_{max} = 18$. The beam propagates along the z-axis. Additionally, the region of interest, which is valid according to the eq. (2.5)(black) and eq. (2.6)(red).

Figure 2.1 shows the effect of choosing different values of n_{max} for an exemplary beam. In the first image $n_{max} = 11$, which leads to $n_{max}^2 + 2 \cdot n_{max} = 143$ for each BSC a and b, so in total 286 complex parameters are used to determine the beam. In the second image $n_{max} = 18$. We observe that for larger n_{max} the beam can be accurately represented in a larger region while the total number of parameters is also substantially increased, up to a value of 720.

The value of n_{max} suitable for our method depends mainly on the location of the camera. For a camera near the target, we must use the field from eq. (2.1), which may result in a high value of n_{max}. However, if the camera is far away we can use the far-field approximation, because all the evanescent modes contribution will be zero, and only use the far-field part of the field. This generally leads to a lower n_{max}, because the region of interest includes only the scatterer.

If the camera is in the near field, we have to cover the domain where the camera resided accurately with our multipole expansion. Hence, the decisive factor for the region of interest is in most calculations the position and size of the camera, but only if the camera is in the near field. It is possible to move the camera into the far-field and thereby lower the necessary n_{max}. The region of interest in the far-field case depends mainly on the size of the scatterer.

A good test to see whether n_{max} is large enough with a camera in the near field is to calculate the camera image and check if the pixel values are changing with higher n_{max}. If n_{max} is sufficiently high, the camera pixel values should not change their values.

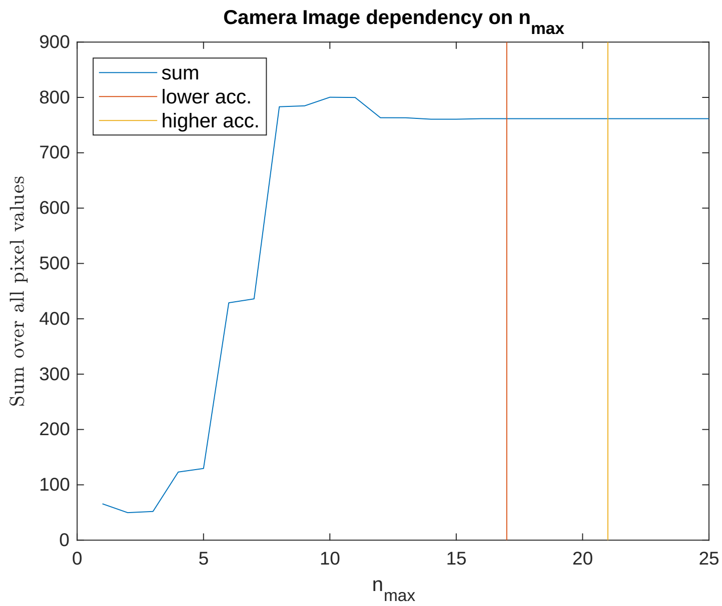

Figure 2.2: **The dependency of the camera image on the number of modes.** In order to determine whether the convergence of the camera image is achieved, we compute the intensity values for every pixel and and add them all up. Doing that for various values of n_{max} confirms that the values converge for a sufficient high n_{max}. Additionally, the values of n_{max} with eq. (2.5)(orange) and eq. (2.6)(yellow) are shown.

Figure 2.2 shows the sum over all pixel values for different n_{max} and we observe that this quantity converges for a high enough n_{max}. Additionally, there are the n_{max} values shown for eq. (2.5)(as a red line) and eq. (2.6)(as a yellow line). Note that for a scatterer with a high refractive index those limits might not be high enough and n_{max} has to be increased further.

2.1.2 Scattering: T-matrix method

The multipole expansion provides us with a method to generate an incoming beam and to accurately represent it. Our attention will now shift towards analysing and understanding the scattering that occurs when a beam interacts with an arbitrary target.

The GLMT is only valid for spherical particles and the scattering can in that case be solved analytically. The scattered field for a target with any arbitrary shape can be calculated with the Transition matrix (T-matrix) method and can be viewed as an extension of the GLMT. The T-matrix gives a relation between the BSCs of the incoming field and the BSCs of the scattered field and can be written as a linear equation

$$\begin{pmatrix} p \\ q \end{pmatrix} = T \begin{pmatrix} a \\ b \end{pmatrix}. \tag{2.7}$$

In general, the T-matrix depends only on the shape, size, composition, and orientation of the particle. Therefore, the T-matrix usually has to be calculated only once and can then be used multiple times for scattering calculations.

To solve the scattering from a particle and calculate a T-matrix, we again split the fields into an incoming, internal and scattered field. The fields have to fulfil the interface boundary condition, which can be derived from Maxwell equations, between the sphere and the environment.

$$\hat{\mathbf{n}} \times (\mathbf{E}_{inc} + \mathbf{E}_{scat}) = \hat{\mathbf{n}} \times \mathbf{E}_{int}, \quad \hat{\mathbf{n}} \times (\mathbf{H}_{inc} + \mathbf{H}_{scat}) = \hat{\mathbf{n}} \times \mathbf{H}_{int} \tag{2.8}$$

This condition leads to the relationship between the incoming, internal, and scattered BSCs, which makes it possible to calculate the T-matrix.

There are many different ways to calculate the T-matrix, depending on the geometry of the scatterer. For a spherical scatterer, the GLMT can still be applied, and represented as a T-matrix. However, it is necessary to employ a numerical algorithm to determine the T-matrix for more complicated shapes [11, 17, 18, 19].

Another important aspect of the T-matrix is that it is also possible to measure the T-matrix in an experiment. The T-matrix can be measured by measuring the outgoing field for all the different incoming modes.

Another valuable quantity that can be derived from the T-matrix is the scattering matrix S. Unlike the T-matrix, which relates the incoming and scattered beams, the scattering matrix describes the relationship between the incoming and outgoing beams. The conversion can be done with

$$S = 2T + I. \tag{2.9}$$

For example, the scattering matrix allows for the computation of the Fisher information operator [5] and generalised Wigner Smith operator [20].

All methods to calculate the T-matrix rely on the assumption that the target is at the origin. But for later calculations, we also need the T-matrix for a target, which is not at the origin such as for evaluating the Fisher information (see sec. 2.2). Calculating the information about a parameter of interest that arrives on a camera screen invokes the derivative of the scattered field with respect to this parameter. Most of the time (in this thesis) this parameter is the position or the orientation of the target, which means that we need a way to shift and rotate the target to calculate the derivative of the T-matrix.

Manipulation of the T-matrix

We want to calculate a modified T-matrix for shifted or rotated targets. Since the T-matrix gives us a relation between the different states that we express using BSCs, we have to study the behaviour of the BSCs under a shift or a rotation.

For a translation along the z-axis, we can calculate the BSCs a', b' with the translation matrices $A(z), B(z)$.

$$a' = A(z)a \quad \text{and} \quad b' = B(z)b \tag{2.10}$$

Those matrices $A(z), B(z)$ are quite complicated to calculate and the derivation is quite involved. In this thesis we will not cover the translation matrices in detail. They can be calculated with the method in [21] or with the method in [22].

For a translation in any arbitrary direction, we can introduce the rotation operation and use a combination of rotation and translation along the z-axis to get a translation in an arbitrary direction. Those beam rotations can be done with the Wigner D-matrices [23] $D(\alpha, \beta, \gamma)$. The Wigner D-matrices are usually known for rotating a quantum state with an angular momentum. However, they can also be used to rotate the states in a multipole expansion of the field. The transformation is given by

$$a' = D(\alpha, \beta, \gamma)a \quad \text{and} \quad b' = D(\alpha, \beta, \gamma)b. \tag{2.11}$$

For the T-matrix we can define different operators, which are composed of those operators, and allow us to directly rotate or translate our particle. The T-matrix can be written with four sub-matrices, each of those sub-matrices acts on one BSC vector

$$\begin{pmatrix} p \\ q \end{pmatrix} = \begin{pmatrix} T_{11} & T_{12} \\ T_{21} & T_{22} \end{pmatrix} \begin{pmatrix} a \\ b \end{pmatrix}. \tag{2.12}$$

With that we can now construct our translation and rotation matrices. For a translation in z direction we get

$$T' = AB(z)^{-1} \cdot T \cdot AB(z) \quad \text{with} \quad AB(z) = \begin{pmatrix} A(z) & B(z) \\ B(z) & A(z) \end{pmatrix}. \tag{2.13}$$

Similarly, we find for the rotation of the T-matrix

$$T' = R(\alpha, \beta, \gamma)^{-1} \cdot T \cdot R(\alpha, \beta, \gamma) \quad \text{with} \quad R(\alpha, \beta, \gamma) = \begin{pmatrix} D(\alpha, \beta, \gamma) & D(\alpha, \beta, \gamma) \\ D(\alpha, \beta, \gamma) & D(\alpha, \beta, \gamma) \end{pmatrix}. \tag{2.14}$$

2.2 Fisher Information

The methods provided so far describe the fields and the scattering from a target, but we want to achieve more than just simulation of the scattering process. Namely, we want to find a beam which generates an intensity distribution that contains the most information about a parameter θ (e.g., position, orientation, etc.) of the target.

Suppose we want to estimate the x-position of our target. The scattered field will depend on the x-position of the target and therefore contains information about the x-position. This information will travel with the electromagnetic wave and part of it will end up on our camera. For the detected intensity on our camera pixel, the scattered field will obey the photon statistics, which is a Poisson distribution with the squared amplitude of the field as the expectation value.

We need statistics to analyse the intensity distribution on the camera. A fundamental tool statistics offers is the Fisher information, which quantifies the ultimate limit to the precision of the measurement.

The Fisher information, named after the statistician Ronald A. Fisher [24], is a fundamental concept in statistics that measures the amount of information about an unknown parameter θ that a random variable X has. Higher Fisher information implies that with the available data we can potentially estimate the parameter θ more precisely.

Single parameter estimation

Suppose we have a data set $X = (x_1, x_2, ..., x_n)$ of size N, which would be in our case the values of the pixels and N the number of pixels. Furthermore, we have a parameter θ, which can be estimated by a function $\hat{\theta}$, the so-called estimator of θ. This function maps our data set to the parameter θ ($\hat{\theta}(X) \approx \theta$). We say that the estimator is unbiased if $b = \mathrm{E}[\hat{\theta}] - \theta = 0$. The estimator for our setup would be a function, which maps a camera image (a data set X) to a position. In practice, such a function can be represented, e.g., by an artificial neural network. Introducing the Fisher information and associated Cramér-Rao bound gives us the opportunity to calculate a lower limit for the variance of the estimator, as we will see in the following.

The Fisher information is defined as the variance of the score function. For a single parameter this leads to this expression

$$\mathcal{I}(\theta) = \int \mathrm{d}\mathbf{x}\, p(\mathbf{x}|\theta) \left[\partial_\theta \log p(\mathbf{x}|\theta)\right]^2 = \mathrm{E}\left[\left(\partial_\theta \log p(X|\theta)\right)^2\right], \tag{2.15}$$

where X is a random variable, θ is an arbitrary parameter and $p(X|\theta)$ is the probability density function.

The Fisher information must satisfy regularity conditions in order to be a valuable quantity with the intended properties. Those regularity conditions are as follows [25]:

- The partial derivative of $p(X|\theta)$ with respect to θ exits almost everywhere.

- The integral of $p(X|\theta)$ can be differentiated under the integral sign with respect to θ.
- The support of the probability distribution $p(X|\theta)$ does not depend on the parameter θ. In other words, the range of values x can take should be the same for all values of θ.

While these conditions are usually satisfied in common parametric models (e.g., normal, Poisson), there are cases where they may fail, requiring more careful analysis. Examples for such distributions where the Fisher information is not defined is a uniform distribution or many other distributions with discontinuities.

Estimation of multiple parameters

For completeness we outline how to deal with multiple parameters. In this thesis, we will stick to one parameter, but in general all of the methods would work also for multiple parameters. The Fisher information for more than one parameter becomes a $N \times N$ positive semidefinite matrix with N being the number of parameters

$$\left[\mathcal{I}(\theta)\right]_{i,j} = \mathrm{E}\left[\left(\frac{\partial}{\partial\theta_i}\log f(X;\theta)\right)\left(\frac{\partial}{\partial\theta_j}\log f(X;\theta)\right)\,\middle|\,\theta\right]. \tag{2.16}$$

The regularity conditions must hold for every component of θ.

2.2.1 The Cramér-Rao Lower Bound

Fisher information is intimately connected with the Cramér-Rao lower bound (CRLB), which provides a lower bound on the variance of unbiased estimators of θ.

Due to its significance, we want to provide a brief derivation of the Cramér-Rao Lower Bound. We follow the derivation given in [26]. Starting with an unbiased estimator we can write

$$\mathrm{E}\left[\hat{\theta}(X) - \theta\right] = \int (\hat{\theta}(x) - \theta)p(x|\theta)\,\mathrm{d}x = 0 \tag{2.17}$$

Appling the partial derivative of θ on both side give us

$$\int (\hat{\theta}(x) - \theta)\partial_\theta p(x|\theta)\,\mathrm{d}x - \int p(x|\theta)\,\mathrm{d}x = 0 \tag{2.18}$$

Rewriting this expression and using $\int p(x|\theta)\,\mathrm{d}x = 1$ and $\partial_\theta p(x|\theta) = p(x|\theta)\partial_\theta(\log p(x|\theta))$ leads to

$$\int (\hat{\theta}(x) - \theta)p(x|\theta)\partial_\theta(\log p(x|\theta))\,\mathrm{d}x = 1 \tag{2.19}$$

Factoring this expression and squaring the whole expression yields

$$\left(\int \left[(\hat{\theta}(x) - \theta)\sqrt{p(x|\theta)}\right]\left[\sqrt{p(x|\theta)}\partial_\theta(\log p(x|\theta))\right]\mathrm{d}x\right)^2 = 1 \tag{2.20}$$

Now we can use the Cauchy-Schwarz inequality, which gives us

$$1 \leq \underbrace{\left[\int (\hat{\theta}(x) - \theta)^2 p(x|\theta)\,\mathrm{d}x\right]}_{\mathrm{Var}(\hat{\theta})} \cdot \underbrace{\left[\int (\partial_\theta \log p(x|\theta))^2\,\mathrm{d}x\right]}_{\mathcal{I}(\theta)} \tag{2.21}$$

Within this formulation, both the variance of the estimator and Fisher information emerge, allowing us to express the Cramér-Rao bound as

$$\mathrm{Var}(\hat{\theta}) \geq \frac{1}{\mathcal{I}(\theta)}. \tag{2.22}$$

This relation marks the importance of the Fisher information in statistics. For an unbiased estimator, the variance cannot be less than the inverse of the Fisher information.

Similar to the Cramér-Rao bound for the single parameter case, there is an inequality equation connecting the Fisher information matrix with the covariance matrix

$$\Sigma^{-1} \succeq \mathcal{I}(\theta), \tag{2.23}$$

where $\succeq$ denotes that the difference $\Sigma^{-1} - \mathcal{I}(\theta)$ is positive semidefinite.

2.2.2 Calculating the Fisher information for the camera

The Fisher information on our simulated camera can be calculated by using a semi classical approach to describe the quantum behaviour of the photons. To describe the discrete nature of photons we model the shot noise by a Poisson distribution

$$p(X|\theta) = \prod_{k=1}^{N} \frac{|E_k^{\mathrm{out}}|^{2x_k} e^{-|E_k^{\mathrm{out}}|^2}}{x_k!}, \tag{2.24}$$

with index k representing the different pixels and $|E_{\mathrm{out}}|^2$ the expected intensity on the camera pixel. In [5], the authors derived an expression for the Fisher information with the shot noise distribution. However, in practical imaging systems, the measurements are further corrupted by additional noise sources, such as readout noise, which comes from thermal fluctuations, electronic noise, etc. We denote this additive noise component as ξ. This readout noise is often assumed to be independent of the intensity and it is usually modelled as a normal distribution ($\xi \sim N(\mu_\xi, \sigma_\xi^2)$).

Following the derivation in appendix B gives us this expression

$$\mathcal{I}(\theta) = \sum_{k=1}^{N} \frac{\left[\partial_\theta(|E_k^{\mathrm{out}}|^2)\right]^2}{|E_k^{\mathrm{out}}|^2 + \sigma_\xi^2}. \tag{2.25}$$

This expression is the Fisher information on the camera for not only a shot noise distribution, but also a mixture of the camera readout noise and the shot noise. Additionally, the σ_ξ can not only denote the standard deviation of the readout noise but can also cover the case, where the pixels have constant background illumination. With that we can cover a wide range of different experimental parameters.

In the expression for the Fisher information, the noise of the camera only enters in the denominator. Without the noise, the Fisher information for some pixel values could diverge. This could happen if the pixel is not illuminated, which leads to division by essentially zero, but the additional read out noise prevents that and leads to a better numerical stability. However, that may result in an alternative maximal state. This will be analysed further in the later section (see sec. 3.2.2), because we are ultimately interested in the Maximum information state (MIS).

To actually calculate the Fisher information we need the derivative of the intensity on a camera pixel with respect to the parameter θ. This can be done numerically in our simulation.

The differential

As we need to do our calculation numerically, we need finite differences to calculate our derivative of the intensity with respect to a parameter θ in eq. (2.25). Using central differences yields the most accurate result and it is, in our case, not much more computationally expensive as the forward/backward differences. Converting the expression for the derivative into central finite differences results in

$$\partial_\theta(\left|E_k^{\text{out}}\right|^2) = \frac{\left|E_k^+\right|^2 - \left|E_k^-\right|^2}{2\Delta\theta}, \tag{2.26}$$

with $\left|E_k^+\right|^2$ being the scattered field with a changed parameter $\theta+\Delta\theta$ of the scatterer and $\left|E_k^-\right|^2$ the same but with $\theta - \Delta\theta$. Putting everything together we get a final expression for our Fisher information

$$\mathcal{I}(\theta) = \sum_{k=1}^{N} \frac{\left[\left|E_k^+\right|^2 - \left|E_k^-\right|^2\right]^2}{2\Delta\theta\left|E_k^{\text{out}}\right|^2 + \sigma_\xi^2}. \tag{2.27}$$

The Fisher information scales linearly with the beam power ($\mathcal{I} \propto |E|^2 \propto P$), which means that a higher power leads to a better beam (in terms of Fisher information). However, due to experimental constraints, such as thermal heating of the scatterer, we seek for a beam that has a large Fisher information content for a fixed level of power. In our optimization procedure we fix the power of the beam by adding a constraint to our cost function (see sec. 3.1 for further details).

With this expression of the Fisher information in our setup it is possible to calculate the Cramér-Rao lower bound and directly bound the performance of the estimation of the parameter of interest θ. This estimation is only a lower bound for the variance and not every estimator reaches the bound. The real measurement precision thus also depends on how the data is processed, however, this analysis will not be covered in this thesis where we regard the precision as a property of the electromagnetic field.

A useful quantity is the normalised Fisher information as it does not depend on the power of the incoming beam. A way to do that is by dividing the Fisher information by the total power

$$N\mathcal{I} = \frac{\mathcal{I}}{P_{tot}}. \tag{2.28}$$

This expression helps to judge the performance of a beam without the influence of the power of the beam. The normalised Fisher information could be used as a cost function. Thus eliminating the need for a constraint for the cost function, but in this thesis we do not use this quantity as our cost function, but as a tool to compare different beams to each other.

Before tackling the problem of finding beams with an maximal amount of Fisher information we need to assess the numerical stability of the expression (eq. (2.27)), which we test using various values for the finite difference step size $\Delta\theta$. This evaluation is presented in Fig. 2.3.

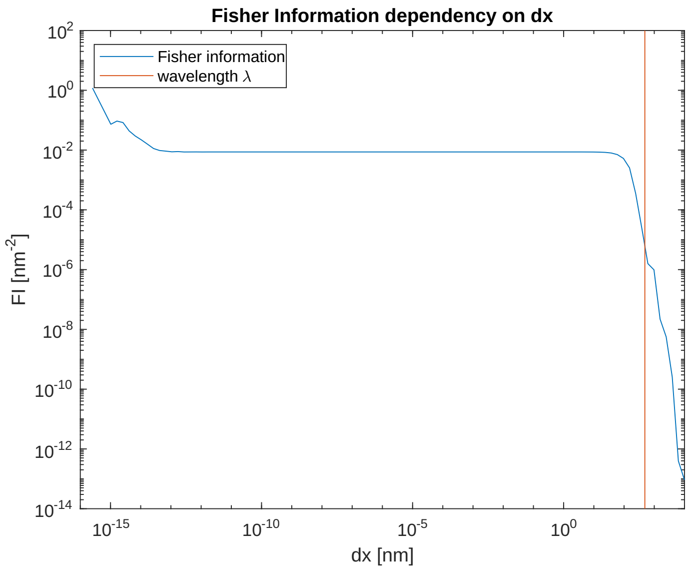

Figure 2.3: **Test of the numerical derivative.** The Fisher information calculated with the central difference method (eq. (2.26)) for different values of $\Delta\theta$ on a log-log plot. In this case, we used the lateral position x as our parameter θ. Additionally, the commonly used wavelength in this thesis $\lambda = 488\,\text{nm}$ is also indicated.

As we see in Fig. 2.3, there is a large interval of $\Delta\theta$, where Fisher information remains constant. At small values of $\Delta\theta$, the derivative within the expression of the Fisher information becomes unstable, leading to divergence for vanishing $\Delta\theta$. For large $\Delta\theta$ values the Fisher information becomes small and does not accurately characterise the derivative. However, there may be other intriguing phenomena that can be observed at larger scales of $\Delta\theta$. There are existing works, which investigate this phenomenon [27], but those lie outside of the scope of this work. For our calculation, we use $\Delta\theta = \epsilon^{1/3} = 6.055 \times 10^{-6}$. With ϵ being the relative floating-point accuracy, which is in our case $\epsilon = 2.22 \times 10^{-16}$.

2.3 Calculation of the Fisher information on the camera for an example beam

In order to gain a better understanding of the methods introduced above, we start with the calculation of the scattering and the resulting Fisher information for an example beam and analyse the results.

Typically, such imaging measurements are carried out by employing the so-called Gaussian beams. For our example, we used a Laguerre-Gaussian beam with an azimuthal and radial mode of zero, the so-called *LG00* beam. This beam is then used to present the workflow and for comparison with our optimised beam, which will be presented in chapter 3.

Our *LG00* beam, has an NA of 0.5 and the wavelength of the beam is 488 nm. The beam is polarized along the y-axis.

The first step in our analysis is to find the BSCs of the incoming *LG00* beam, so that we can represent the beam and calculate the corresponding fields. After that we can introduce a target, which scatters the light. For that we need to calculate the T-matrix, which depends on the geometry and the material.

With all of that, we are capable of calculating the field scattered by the target. The next thing to do is to place a camera somewhere in the vicinity of the target and calculate the spatial distribution of the intensity projected onto the camera. Moreover, we need to repeat this procedure for two more target positions that are slightly shifted compared to the original target. The Fisher information is then calculated from the resulting intensity distribution on the camera.

2.3.1 Multipole Expansion

As explained in sec. 2.1, to calculate the electromagnetic field of the beam with the multipole expansion, we need the BSCs of the field.

Those BSC can be calculated by different methods depending on the type of the beam (see sec. 2.1.1).

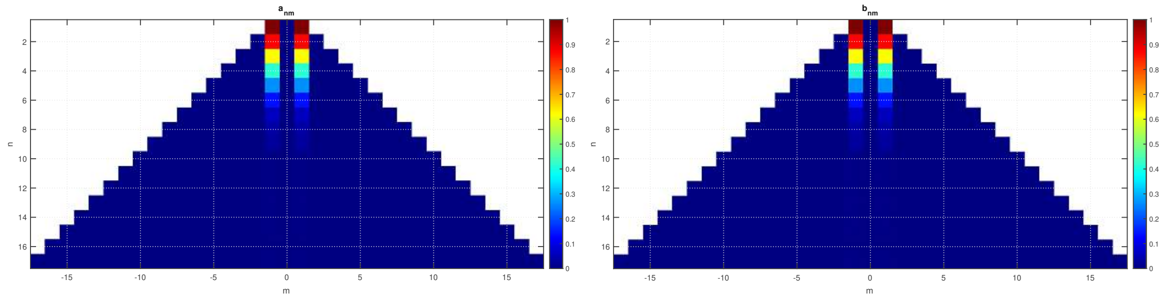

Figure 2.4: **BSCs for a *LG00* beam**. Those BSCs are generated with the point matching method provided by the OTT Toolbox [12]. Each rectangle at an integer point of n (y-axis) and m (x-axis) corresponds to one BSC. In the first figure are the BSC corresponding to the electric modes. In the second figure are the BSC for the magnetic modes. n is limited by n_{max} and every n mode has $m = 2n + 1$ modes.

Figure 2.4 shows the BSCs for the *LG00* beam. The first plot in this figure depicts a_{nm}, which corresponds to electrical modes, and the second one b_{nm}, corresponds to magnetic modes. For this instance, we use $n_{max} = 17$, resulting in $n_{max}^2 + 2 \cdot n_{max} = 323$ modes for each BSC. Most of the modes are close to zero and only the modes with a low n are non zero. This is because our *LG00* beam is focused and only has a field around the origin.

With the multipole expansion of the target beam, we proceed with computing the T-matrix for our scattering object. In this instance, we consider a sphere with a radius of 100 nm and a refractive index of 1.44. As detailed in sec. 2.1.2, the T-matrix can be derived through several approaches, but for a spherical object, the GLMT is applicable.

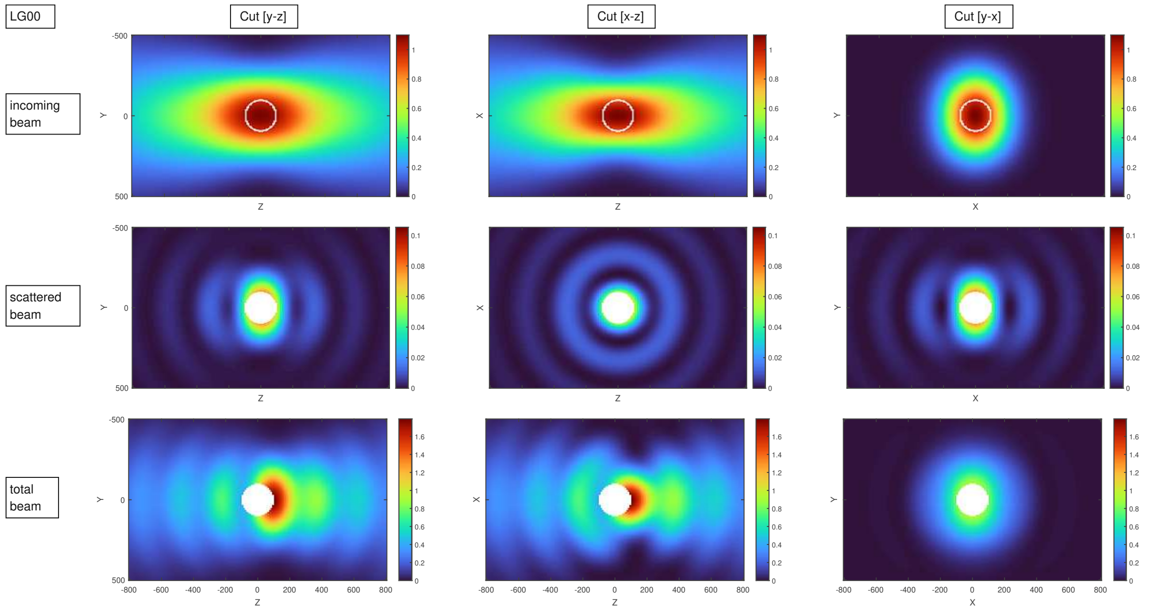

Figure 2.5: **Various plots of the *LG00* beam.** The three different columns represent spatial cuts [y-z], [x-z] and [y-x] respectively. The first row shows the *LG00* beam with no scattering, but the scatterer is shown as a thin outline. Second row shows the scattered part of the beam and the third row is the total beam, which is the sum of the incoming and scattered beam. The colour map shows the intensity of the field. The scatterer is a sphere with a refractive index of $n = 1.44$ and a radius of $r = 100\,\mathrm{nm}$. The beam comes from left side ($z = -\infty$).

Figure 2.5 shows a *LG00* beam both with and without scattering. Using this data, we can derive the image on the simulated camera, subsequently compute the Fisher information, and evaluate the beam's performance.

2.3.2 Fisher information

The Fisher information for a specific parameter θ, which in this context is the lateral center of mass position of the scattering object x, can be derived from the camera image (see 2.2.2). In this configuration, the camera has a numerical aperture (NA) of 0.75, leading to a camera length of 1133 nm, positioned 500 nm away from the target center. The number of pixels is $32 \times 32 = 1024$.

Equation (2.1) computes the field at each individual pixel k at position $\mathbf{r}_k$, but for our camera we need the intensity of this field, which is given by $I = |E|^2$. Due to the derivative and the choice to use the central differences, this is done three times, with a scatterer at the origin and then the same scatterer at a slightly different position $x \pm \Delta x$. With that we can calculate the Fisher information on the camera as explained in 2.2.2.

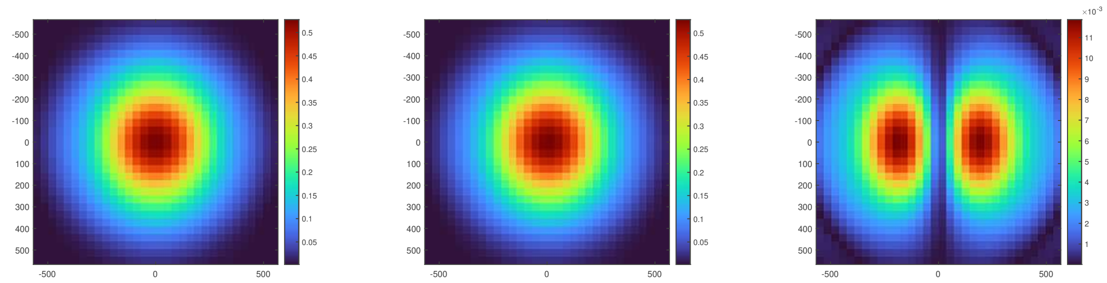

(a) **Camera image($x = 0$)** The calculated camera image with the scatterer at the origin.

(b) **Camera image($x = \Delta x$)** The calculated camera image with the scatterer slightly translated.

(c) **Difference** The absolute difference of the camera images in (a) and (b).

Figure 2.6: **Effect of a small change in the position.** A way to visualise the performance of a beam is to look at the difference a small change has on the outgoing field.

Figure 2.6 illustrates (a) the camera image produced from a scatterer at the origin, (b) the camera image produced from a scatterer with a slightly shifted lateral position $\Delta x = 10\,\mathrm{nm}$, and (c) the difference between those two images. The difference between the camera image already gives us insight as to whether the beam is good for measuring the lateral position x. If there are no or only small changes, it will be difficult to differentiate those images and therefore difficult to measure the position. However, if these changes are large, the position can be measured precisely. It should be noted that these differences do not represent the Fisher information per pixel[1].

With the camera in place, it is possible to calculate the Fisher information. As explained in the previous section the Fisher information scales linearly with the power, but we do not want to compare beams with different powers. Therefore, we use the normalised Fisher information $N\mathcal{I}$[2].

$$N\mathcal{I} = 1.85 \times 10^{-6} \tag{2.29}$$

In the following, we answer the question whether there are other beams, different from the common Laguerre-Gaussian beam, that are better in terms of Fisher information. In particular, we search for the optimal beam in that regard.

[1] The Fisher information per pixel is the relative change in the camera image. If the pixel is already highly illuminated the Fisher information would be low.

[2] With that result and assigning the appropriate power, it is possible to calculate the Cramér-Rao lower bound (see 2.2.1), i.e., a lower bound of the variance of the lateral position x for a given power. The normalised Fisher information, however, should not be converted to a CRLB.

3 Optimising the Fisher Information

In this chapter, we will introduce our optimisation algorithm that we use to find the maximum information states, i.e., the states that direct a maximum amount of information about a parameter of a scattering object onto a camera. First, we test our new method on a simple case using a sphere as the scatterer. Following this, we apply the method to a thin cylinder as the scatterer, inspired by [7], where they measured the position of a thin nanowire.

3.1 Optimisation method

The objective of the optimisation is to maximise the Fisher information captured by the camera. This is achieved by systematically varying the BSCs of the incident beam and computing the resultant scattered field. This computational approach enables us to generate the corresponding camera image and subsequently determine the Fisher information for the given beam. As explained in 2.2.2, the Fisher information increases linearly with the power of the beam. Therefore, we incorporate a constraint within the cost function of our optimisation to ensure constant power throughout the process and prevent any divergence in the power of the beam. The optimisation problem can be stated as

$$\max_{a_{\text{in}}, b_{\text{in}}} \quad \mathcal{I}(\theta, a_{\text{in}}, b_{\text{in}}) \tag{3.1a}$$

$$\text{s.t.} \quad P_0 - P(a_{\text{in}}, b_{\text{in}}) = 0 \tag{3.1b}$$

whereby $P(a, b)$ is the power of the beam for a given set of BSCs a and b, P_0 is the power of the initial beam as given in eq. (2.2) and the expression for the Fisher information is the same as in eq. (2.27). The BSCs a and b enter the Fisher information $\mathcal{I}(\theta, a_{\text{in}}, b_{\text{in}})$ via the electric field.

In order to find the best incoming beam, i.e., the BSCs a_{in} and b_{in}, for a given power, we need a machine learning algorithm. We used Matlab's *fmincon* with the *interior-point* method [28, 29] as our optimisation algorithm. In this thesis, we will not have any constraints on the direction of the incoming beam, which means that all physical solutions can be reached. However, creating such a beam might not be possible in the experiment.

In appendix E there is a summary and description of the parameters used in our calculations. Most optimisation runs were done on the Vienna Scientific Cluster (VSC).

3.2 Maximum information states for a sphere

The first optimisation run is with a sphere as a scatterer. All parameters are kept the same as in the example with the LG00 beam (see 2.3), so that we can compare the results and see the difference in performance.

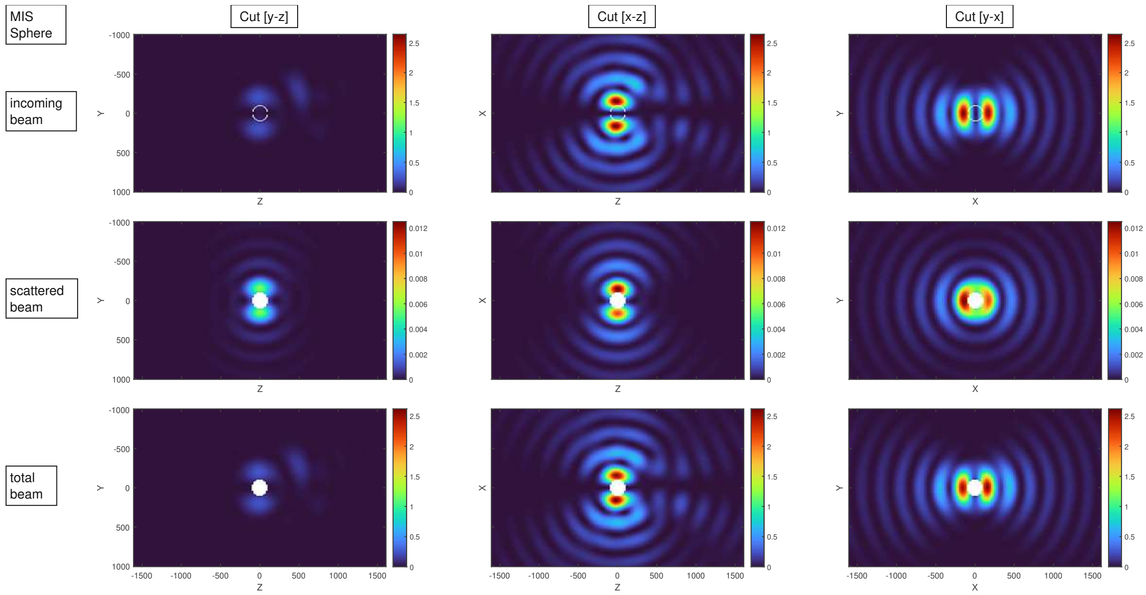

Figure 3.1: **Various plots for a MIS.** The three different columns represent spatial cuts [y-z], [x-z] and [y-x] respectively. The first row shows the MIS for a sphere with a refractive index of $n = 1.44$ and radius of $r = 100\,\text{nm}$ with no scattering, but the scatterer is shown as a thin outline. Second row shows the scattered part of the beam and the third row is the total beam, which is the sum of the incoming and scattered beam. The colour map shows the intensity of the field. The MIS is not constrained to any particular direction during the optimisation.

Figure 3.1 shows the MIS to measure the lateral position x of a sphere with a radius of 100 nm. The physical interpretation of this state is that it has two maxima on each side of the x-axis of the target and with no displacement there is little scattering. A slight displacement of the target along the x-axis results in placement in the maximum and therefore increases the scattering, which can be measured on the camera.

Another interesting characteristic of the MIS is that the scattered beam has a similar shape to the incoming beam. The MIS for this setup is thus a beam that is almost non-interacting with the target when the target is at the position for which the optimisation is performed. Although this might seem at the first glance to be a beam that carries no information to the camera, one should keep in mind that the Fisher information is not determined by the intensity on the camera but by its change as the position of the scatterer is slightly varied.

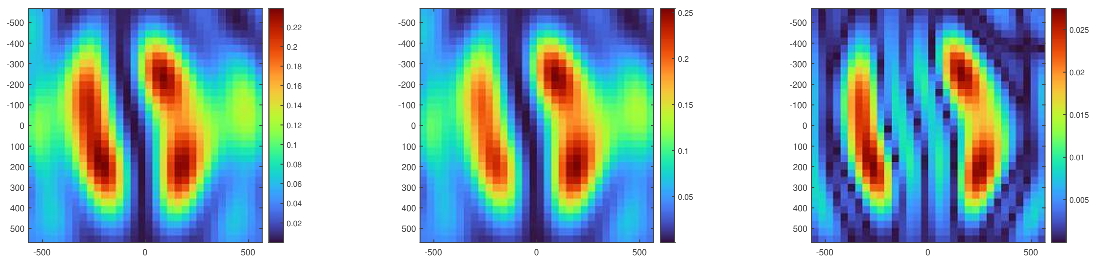

(a) **Camera image($x = 0$)** The calculated camera image with the scatterer at the origin.

(b) **Camera image($x = \Delta x$)** The calculated camera image with the scatterer slightly translated.

(c) **Difference** The absolute difference of the camera images in (a) and (b).

Figure 3.2: **Effect of a small change in the position.** A way to visualise the performance of a beam is to look at the difference a small change has on the outgoing field. For that we depict three different camera images, where the colour map shows the intensity. In (a) is the camera image with the scatterer at the origin. In (b) is the camera image with the scatter slightly shifted from the origin and in (c) is the absolute difference between (a) and (b).

Figure 3.2 shows, similarly to Fig. 2.6, three different camera images when the scatterer is illuminated with the MIS. The first one 3.2 (a) is the camera image with the target at the origin and 3.2 (b) is the camera image with the target slightly translated in the x-direction ($x = \Delta x = 10\,\mathrm{nm}$). In 3.2 (c) is the the difference between (a) and (b) depicted. If the difference is higher for small change in the parameter of interest θ (in this case x) it is in general easier to measure that parameter.

Comparing this result with a *LG00* beam we can see that we have a higher difference and thus higher Fisher information. Calculating the normalised Fisher information leads to

$$N\mathcal{I} = 4.24 \times 10^{-4}. \tag{3.2}$$

If we compare this with the previous result by calculating the ratio

$$\eta = \frac{N\mathcal{I}_{MIS}}{N\mathcal{I}_{LG00}} = 229, \tag{3.3}$$

we observe that the optimisation allows for a substantial increase of the Fisher information (by two orders of magnitude), hence for a much better measurement precision of the position of the sphere. A question that remains is whether this MIS is actually the optimal beam or if there exist better beams that we could not find with our optimisation.

3.2.1 Checking the optimisation with different initial conditions

A key test for the optimisation method is to examine its behaviour when the same setup is used but with varying initial conditions (the BSCs at the beginning of the optimisation). In the optimal case we should find the same global maximum for all different initial conditions. Although we are not able to prove that our optimised beam is a global maximum, our check serves as a strong indication that our optimisation method produces beams, which are close to the global maximum.

We generate our different initial conditions by drawing from a uniform distribution between -1 and 1 for the real and imaginary part of the BSCs

$$a_{nm} \in U(-1,1) + \mathrm{i} \cdot U(-1,1) \tag{3.4a}$$

$$b_{nm} \in U(-1,1) + \mathrm{i} \cdot U(-1,1) \tag{3.4b}$$

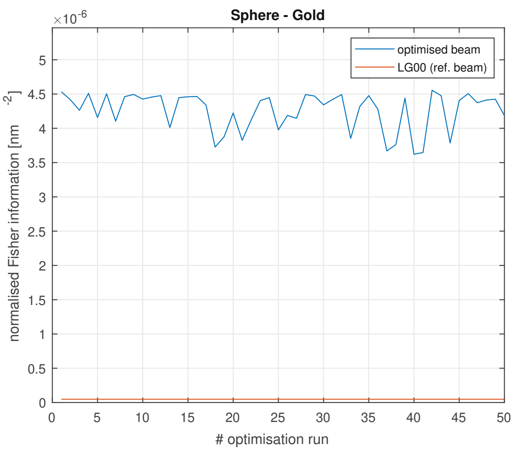

(a) **Setup 1**
In the first setup we use a gold sphere with a radius of $r = 100\,\mathrm{nm}$ and a wavelength of $\lambda = 488\,\mathrm{nm}$.

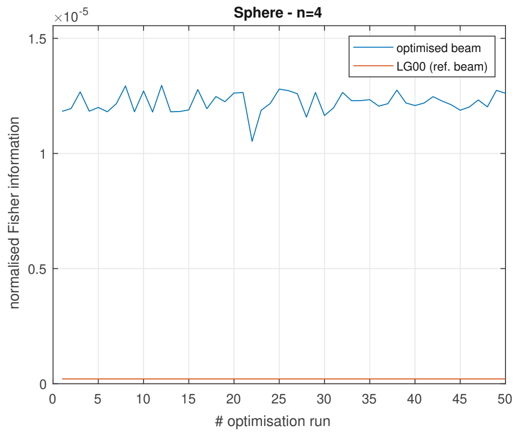

(b) **Setup 2**
In the second setup we use a sphere with a radius of $r = 100\,\mathrm{nm}$, a refractive index of $n = 4$ and a wavelength of $\lambda = 620\,\mathrm{nm}$.

Figure 3.3: **Fisher information for different initial conditions.** We use two different setups to check the results from the optimisation method. Both setups are probed with 50 initial conditions and, as can be seen, the Fisher information is almost constant across those runs.

Figure 3.3 shows the Fisher information for the different optimisation runs using two different setups. In 3.3(a) we show the results for a gold sphere with a radius of $r = 100\,\mathrm{nm}$ as a target and a wavelength for the incoming light of $\lambda = 488\,\mathrm{nm}$ depicted and in 3.3(b) we show the results for a sphere with a refractive index of $n = 4$ and a radius of $r = 100\,\mathrm{nm}$. The incoming light has a wavelength of $\lambda = 620\,\mathrm{nm}$.

In the first setup, we observe that the Fisher information does not change much. The mean value of the Fisher information is $\overline{N\mathcal{I}} = 4 \times 10^{-6}$ with a standard deviation of $\sigma_{N\mathcal{I}} = 2.81 \times 10^{-7}$. The second setup has in general a higher Fisher information, because the fields scatter more on that target (see chapter 4), but the overall Fisher information for all optimisation runs is relatively constant with a mean value for the Fisher information of $\overline{N\mathcal{I}} = 1.22 \times 10^{-5}$ and a standard deviation of $\sigma_{N\mathcal{I}} = 4.43 \times 10^{-7}$.

In appendix F.1 we show some of the MIS for each setup. It turns our that there is no big difference between the different MIS.

3.2.2 Maximum information states dependency on the noise

Another important test is the dependency of the MIS on the noise. We want to check whether the same input state maximises the Fisher information regardless of the strength of the readout noise σ_ξ^2. Starting with the simpler case of the Fisher information for one pixel. This problem can be formulated as

$$\arg\max(f(x)) \stackrel{?}{=} \arg\max(g(x)) \tag{3.5}$$

with

$$f(x) = \frac{\partial_\theta(x)^2}{x + \sigma_\xi^2} \quad \text{and} \quad g(x) = \frac{\partial_\theta(x)^2}{x + \sigma_\xi^2 + \delta\sigma_\xi^2}. \tag{3.6}$$

With that we can now write

$$g(x) = h(f(x)), \tag{3.7}$$

whereby the function h transforms our initial function into a function with a new value for σ_ξ. If and only if the function h is strictly monotonically increasing, which means if $\alpha < \beta$ this implies $h(\alpha) < h(\beta)$, is eq. (3.5) a true statement. The function h is then called an order-preserving function [30]. We find that h is given by

$$h(y) = \frac{y \cdot \partial_\theta(x)^2}{\partial_\theta(x)^2 + y \cdot \delta\sigma_\xi}. \tag{3.8}$$

We can now check, whether $h(y)$ it is monotonically increasing by writing

$$h(\alpha) < h(\beta). \tag{3.9}$$

Inserting for $h(\alpha)$ and $h(\beta)$ leads to

$$\frac{\alpha \cdot \partial_\theta(x)^2}{\partial_\theta(x)^2 + \alpha \cdot \delta\sigma_\xi} < \frac{\beta \cdot \partial_\theta(x)^2}{\partial_\theta(x)^2 + \beta \cdot \delta\sigma_\xi}. \tag{3.10}$$

Dividing both side with $\partial_\theta(x)^2$ does not change the order because $\partial_\theta(x)^2 > 0$ is always fulfilled in our case. This leads to

$$\frac{\alpha}{\partial_\theta(x)^2 + \alpha \cdot \delta\sigma_\xi} < \frac{\beta}{\partial_\theta(x)^2 + \beta \cdot \delta\sigma_\xi}. \tag{3.11}$$

Furthermore, is the expression $\partial_\theta(x)^2 + y \cdot \delta\sigma_\xi > 0$ because otherwise the function $h(y)$ would become negative and we would receive negative Fisher information, which cannot happen. With that we get

$$\alpha\partial_\theta(x)^2 + \alpha\beta \cdot \delta\sigma_\xi < \beta\partial_\theta(x)^2 + \alpha\beta \cdot \delta\sigma_\xi. \tag{3.12}$$

From this expression it can be easily seen that

$$\alpha < \beta. \tag{3.13}$$

It can also be seen that this function is strictly monotonically increasing, which leads to

$$\arg\max(f(x)) = \arg\max(g(x)) \tag{3.14}$$

This shows us that the MIS maximises the Fisher information regardless of the value of σ_ξ^2 for one pixel. This insight is particularly relevant in the context of single-pixel imaging, where maximising information extraction from limited measurements is essential. Those single-pixel imaging techniques are commonly used in the Terahertz regime, where sensor arrays are hard to make.

Now we generalise the result for a single pixel to the whole camera image. For that we define two new functions with $\mathbf{x}$ being our camera image with size N

$$\bar{f}(\mathbf{x}) = \sum_{i=1}^{N} f_i(\mathbf{x}) = \sum_{i=1}^{N} \frac{\partial_\theta(\mathbf{x}_i)^2}{\mathbf{x}_i + \sigma_\xi^2} \quad \text{and} \quad \bar{g}(\mathbf{x}) = \sum_{i=1}^{N} g_i(\mathbf{x}) = \sum_{i=1}^{N} \frac{\partial_\theta(\mathbf{x}_i)^2}{\mathbf{x}_i + \sigma_\xi^2 + \delta\sigma_\xi^2} \tag{3.15}$$

In general the maximum state is not

$$\left[\arg\max(\bar{f}(\mathbf{x}))\right]_i \neq \arg\max(f_i(\mathbf{x})). \tag{3.16}$$

This tells us that the pixel i does not have to be at the maximum, rather the collective sum should be maximised. For example, if one pixel i cannot achieve a high Fisher information, because it is somewhere at the edge of the camera or it is highly illuminated, it is not useful to maximise this pixel. In appendix C we give a more detailed analysis of this calculation. In general we cannot state that our MIS also maximises the Fisher information for different noise σ_ξ^2. In this thesis we will not investigate different values for σ_ξ^2 and just stick to one value for $\sigma_\xi^2 = 0.095$.

3.3 Maximum information states for a cylinder

The optimisation can be done for various shapes and sizes, as long as the T-matrix can be calculated. In [7] the authors showed experimentally that a specially designed beam (a superoscillatory beam) can improve the measurement of the position of a thin nanowire. By employing a setup similar to their experiment, we are able to compute the MIS for it. Our goal here is to find a beam that allows for further improvement upon the techniques that already exist, ultimately leading to advancements in metrology.

It is worth noting that our simulation offers an idealised representation, providing valuable insights while differing slightly from the experimental setup. Especially for the scatterer itself, in the experiment, they used a wire, which is much longer than it is wide. In the simulation, we use a 200 nm wide and 800 nm long gold cylinder. In contrast to the experimental setup, where the wire was 200 nm wide and 17 µm long. The wavelength of the field is $\lambda = 488\,\mathrm{nm}$. The refractive index of gold at that wavelength is $n = 1.127 + \mathrm{i} \cdot 1.838$. The camera with 100×100 pixels is placed at a distance $d = 500\,\mathrm{nm}$ away from the centre of origin.

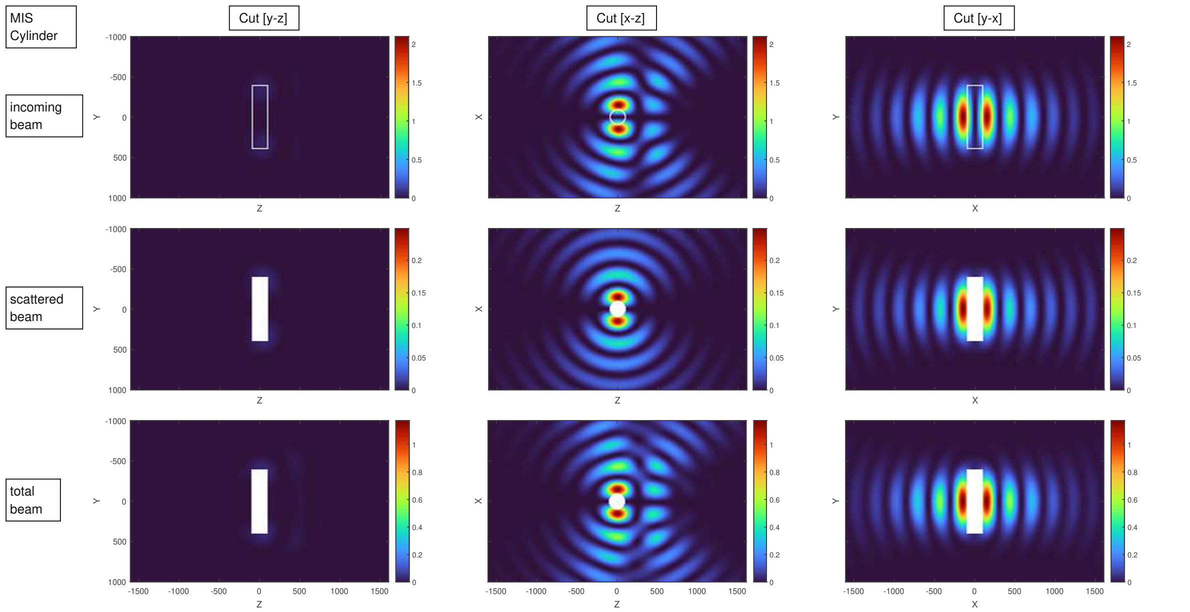

Figure 3.4: **Various plots for a MIS.** The three different columns represent spatial cuts [y-z], [x-z] and [y-x] respectively. The first row shows the MIS for a cylinder with a refractive index of $n = 1.127 + \mathrm{i} \cdot 1.838$, radius of $r = 100\,\mathrm{nm}$ and a height of $h = 800\,\mathrm{nm}$ with no scattering, but the scatterer is shown as a thin outline. Second row shows the scattered part of the beam and the third row is the total beam, which is the sum of the incoming and scattered beam. The colour map shows the intensity of the field. The MIS is not constrained to any particular direction during the optimisation.

Figure 3.4 shows the results of the optimisation with a cylinder with a height of 800 nm and a radius of 100 nm. Similarly to the MIS of the sphere, the resulting beam has two maxima on each side. This result can be expected due to the similarity of the setup and the target, even though the target has a different shape, the physical interpretation is the same. If the target is at the origin there is only little scattering, but if the target is slightly shifted it will scatter much more and therefore result in a huge difference in the camera image.

A rather important observation is the fact that the MIS does not take advantage of the finite length of this cylinder. This observation leads to the conclusion that this beam also produces a high Fisher information for a thin wire, i.e., a cylinder that is much longer.

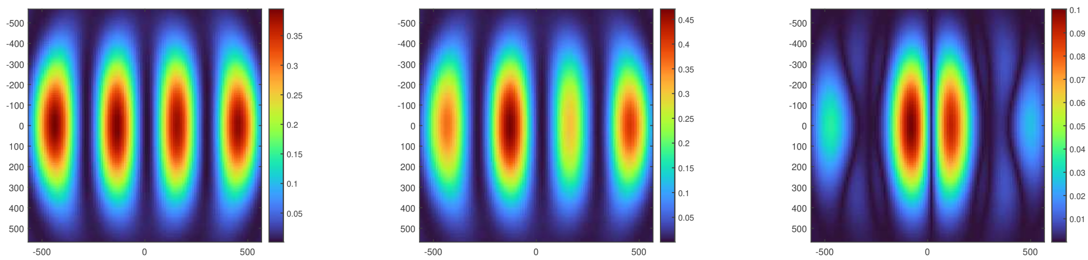

(a) **Camera image($x = 0$)** The calculated camera image with the scatterer at the origin.

(b) **Camera image($x = \Delta x$)** The calculated camera image with the scatterer slightly translated.

(c) **Difference** The absolute difference of the camera images in (a) and (b).

Figure 3.5: **Effect of a small change in the position.** A way to visualise the performance of a beam is to look at the difference a small change has on the outgoing field. For that we depict three different camera images, where the colour map shows the intensity. In (a) we show the camera image with the scatter at the origin. In (b) we show the camera image with the scatter slightly shifted from the origin and in (c) we show the absolute difference between (a) and (b).

Figure 3.5 shows the three camera images for (a) not shifted target, (b) slightly shifted target and (c) the difference of the previous two images. Comparing this to the camera images for the MIS of the sphere shown in Fig. 3.2, it can be seen that there is a completely new pattern emerging even though the beams look rather similar.

We can again calculate the normalised Fisher information, which leads to

$$N\mathcal{I} = 3.9 \times 10^{-3}. \tag{3.17}$$

Comparing this to the previous result for the sphere eq. (3.2) it can be seen that the Fisher information for the cylinder is higher. This result is not surprising, because of the different scatter and, more importantly, the increased number of pixels for the camera (see appendix E).

A different perspective of the beam performance can be obtained by comparing it with the experiment [7]. As we will see in the next section 3.3.1, we can assign a power to the MIS and calculate the lowest possible standard deviation for an estimator with the Cramér Rao bound. With that we can also check whether our optimisation is able to outperform the superoscillatory beam and if so what the theoretical limit would be for such a measurement.

3.3.1 Comparison with the superoscillatory beams

As explained in the beginning of this section, we chose our parameters to match the experiment in [7]. Now we want to compare our MIS to the results from the experiment.

Experimental Setup

In the experiment[7], the authors measured the position of a 17 µm long and 200 nm wide nanowire. This nanowire is generated by cutting the 50 nm Si_3N_4 membrane coated with 65 nm gold layer with a focused ion beam. This leads to a gap of 100 nm from the nanowire to the membrane on both side.

The position of the nanowire can be controlled by applying DC-voltage across the gap. For the illumination of the sample they used a plane wavefront (defocused Gaussian) and a superoscillatory wavefront created with a spatial light modulator (SLM) with a wavelength of $\lambda = 488$ nm. The camera was placed roughly $d \approx 500$ nm away from the nanowire. The estimation of the position of the nanowire from the collected camera images was done by employing a neural network. They used 80% of the data to train the neural network and the remaining 20% to measure the position.

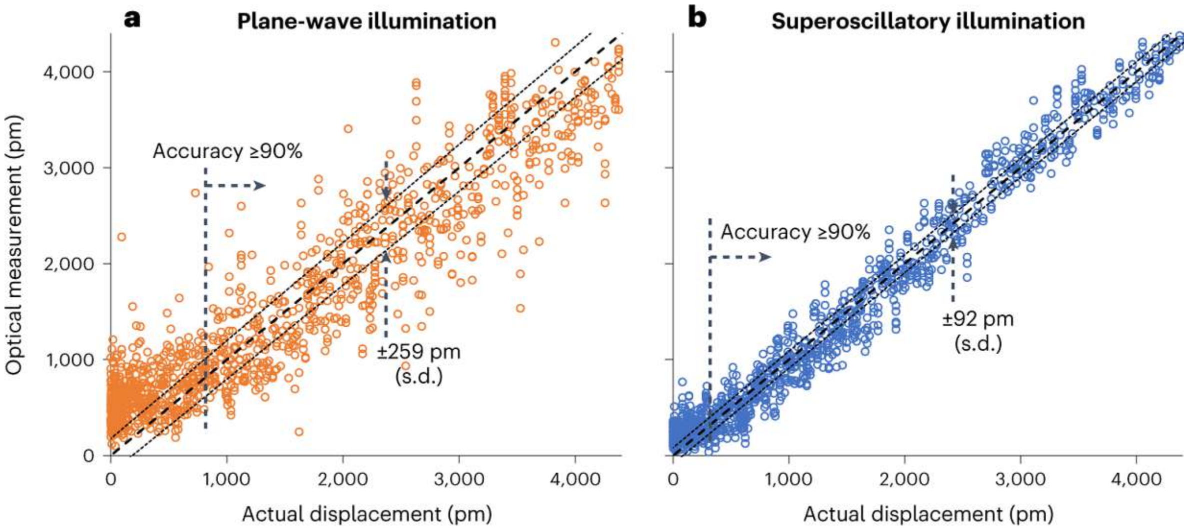

Figure 3.6: **Measurements from an actual experiment [7].** Actual displacement controlled by applying a DC-voltage versus the measured displacement from the camera image. This was be done for (a) a plane wave and (b) a superoscillatory wave.

Figure 3.6 shows the experimental data obtained in the experiment from [7]. The results show that the superoscillatory wavefront can achieve a precision of 92 pm and provides better results than the plane wavefront with a precision of 259 pm.

With this remarkable result, we can compare the MIS and the superoscillating beam in our simulation. The authors of [7] kindly provided us with a SLM pattern they used for the superoscillating beam in the experiment.

Simulation

We calculate the BSCs for the three different beams (plane wave, superoscillatory beam and MIS). The BSCs of a plane wave are straightforward to calculate (see eq. (2.3)), as well as the BSCs for the MIS, which are directly given by the optimisation. The BSCs for the superoscillatory wavefront can be calculated using the OTSLM Toolbox [31] and the SLM pattern.

As we have done before, we calculate the Fisher information on the camera for all three beams. The scatterer we use is a cylinder made out of gold with a radius of 100 nm and a height of 800 nm, which is the same as in the previous section 3.3. The power of the beam was normalised such that the calculated standard deviation of the plane wave has the same value as the result from the plane wave in the experiment. All of the results are presented in the tab. 3.1.

Name	**Fisher info.** [1/nm^2]	**Var.** [nm^2]	**std. deviation** [pm]
Plane wave	14.91	0.067	259
superoscillatory beam	133	0.007516	86.7
MIS	2369.7	0.000422	20.54

Table 3.1: **Calculated values for different quantities for different beams.** In our simulation we can generate all three different beams and calculate the Fisher information. With the appropriate power of the beam, we can calculate the variance and standard deviation.

Table 3.1 shows the results for the Fisher information on the camera, the lowest possible variance of an estimator and standard deviation from such an estimator. The red marked standard deviation of the plane wave indicates that we used this quantity to normalise the power. As we see, the standard deviation of the simulation is almost the same as in the experiment, which is a really promising result. However, this similarity of our simulation and the experiment should be studied more carefully before making the claim that our simulation depicts the reality in this precision. There are a few approximations and differences to the experiment, which are being neglected in our simulation, such as geometry of the camera and number of pixels. Generally speaking, however, the standard deviation of the MIS is quite a bit lower than that of the superoscillatory beam, which shows that our optimisation works very well.

3.4 Summary and discussion

In this chapter we described the optimisation method and did the first optimisation for a sphere with the parameter of interest being the lateral position. The results we got significantly outperformed a conventional Laguerre-Gaussian beam, which shows the potential of our method. However, alternative approaches to this optimisation are possible. We want to highlight other possible approaches to solve the optimisation problem that were employed recently to solve related problems:

In [32] the authors performed an optimisation for an incoming beam which maximises the trapping stiffness of the beam for a particular particle. In contrast to our optimisation problem, they did not use the BSCs as the varying parameter. Instead, they built a Bessel beam basis and used the coefficient vector for the optimisation.

In [33] the authors looked at the outgoing intensity distribution in a multimode fiber with a distinct perturbation (i.e., local deformation). In this setup, they identified the maximum intensity channel which maximises the change in the output intensity distribution inflicted by a perturbation. The method they used to maximise the Fisher information was a higher order singular value decomposition (HOSVD).

Both of them would be valid options, but we regard our approach as straightforward due to its simplicity. An important note is that our MIS are physically valid states, but it may not always be possible to reconstruct those in the experiment, in particular, the SLM needed for such a beam is not trivial to construct. Such a SLM would require an additional algorithm for their generation. This would be easier with a Bessel beam basis, but the Bessel beam basis might not cover the whole space of possible beams. In general, we can achieve experimentally feasible results by incorporating physical constraints into our optimisation routine, e.g., by only optimising a relevant subset of the parameters.

After the first optimisation, we showed that our optimisation always gives us the same MIS with a similar Fisher information for the same setup regardless of the initial condition, which tells us that the optimisation method most likely arrives at a global maximum. After that we looked at the impact of the additive noise we introduced in our probability distribution (see sec. 3.2.2). The noise does not change the MIS for a single pixel measurement, which is a nice feature of the MIS. However, the whole camera image might change the MIS, but this needs a more detailed calculation and is not fully covered in this thesis.

The second optimisation we did was for a cylinder as a target. We used a similar setup as used recently in an experiment [7], where the position of a gold wire could be measured with great precision using a superoscillatory beam. Our results from the optimisation achieved a beam, which performed really well in the simulation and even outperformed the superoscillatory beam.

In summary we can say, that both (cylinder and sphere) optimisation runs generate a beam, which has a high Fisher information on the camera. However, the two MISs, for the sphere and cylinder respectively, look rather similar to each other, although we have two different types of scatterers. It seems that they make use of the same physical properties to generate the Fisher information. This leads to the question, whether this is always the best beam or if there are other types of beams for a different setup. Furthermore, we want to know what is the dependency of the Fisher information for the MIS on different system parameters, e.g., wavelength of the incoming beam, size of scatter, the position and size of the camera, etc.

4 The Fisher information and its dependency on different system parameters

Building on the promising results obtained from the first setups, this chapter extends the analysis by conducting further optimisation runs. Our aim is to investigate the impact of varying system configurations and to gain deeper insights into how different parameters influence the Fisher information and the MIS. The MIS are always very specific to the experimental setup at hand. In the optimisation, we take into account not only the measurement noise mechanism but also the parameters of our system such as the placement of the scatterer and the camera, the size of the camera, the wavelength of the light, etc. The resulting MIS are thus fine-tuned for the physical setup and might look very different when the setup is changed. While this approach is certainly optimal if the specifics of the experiment are known, we want to go one step further and ask the question if we can distill general features of the MIS that apply to various setups and if we can understand the physical effects that generate the Fisher information. Therefore, we explore the MIS for various setups and observe how the optimal state changes as system parameters are varied.

Some interesting system parameter, which we can vary are the wavelength and the size of the scatterer. Those two will be investigated in this chapter for different scatterers. An important quantity to look at when we vary the wavelength of the incoming light or the size of the scatterer, respectively, is the cross section. The cross sections are a well-known quantity and the total cross section is the sum of the cross sections of different processes. In this thesis, the quantities we will look are the scattering and absorption. With that we can calculate the scattering cross section, absorption cross section and the extinction cross section, which is the sum of the scattering cross section and the absorption cross section. In particular, the scattering cross section (SCS) will be of great interest to us. With higher SCS we expect to have a higher Fisher information. This is because with a higher SCS the incoming field scatters more strongly and thus a stronger signal can arrive at the detector.

4.1 Cross section

We start with the description of the cross section, which can be calculated by looking at the time average Poynting vector

$$\langle \mathbf{S} \rangle = \langle \mathbf{S}_\mathrm{i} \rangle + \langle \mathbf{S}_\mathrm{s} \rangle + \langle \mathbf{S}_\mathrm{ext} \rangle, \tag{4.1}$$

where $\langle \mathbf{S}_\mathrm{i} \rangle$ is the incoming, $\langle \mathbf{S}_\mathrm{s} \rangle$ is the scattered and $\langle \mathbf{S}_\mathrm{ext} \rangle$ is the extinguished density of energy flow and $\langle \cdot \rangle$ denotes the time average. Following the derivation in [34], we can then express the cross section as

$$Q_\mathrm{ext} = Q_\mathrm{s} + Q_\mathrm{a} = \frac{4\pi}{k} \,\mathrm{Im}\left\{ \frac{\mathbf{E}_\mathrm{i} \cdot \mathbf{E}_\mathrm{s}^{(0)}(\mathbf{k}_i/k)}{E_\mathrm{i}^2} \right\}, \tag{4.2}$$

whereby $\mathbf{E}_\mathrm{i}$ is the amplitude of the incoming wave, $\mathbf{E}_\mathrm{s}^{(0)}$ is the scattering amplitude and k is the wave vector. This result constitutes the optical theorem. The optical theorem relates the total cross section to the zero-angle amplitude. In this calculation we only considered scattering and absorption, so our total cross section is equal to the extinction cross section. Furthermore, we can now express the cross sections also with the BSCs, which yields for the scattering cross section (SCS)

$$Q_s = \frac{2}{a^2 k^2} \sum_{n=1}^{\infty} (2n+1) \left(|a_n|^2 + |b_n|^2 \right), \tag{4.3}$$

and for the extinction cross section

$$Q_e = \frac{2}{a^2 k^2} \sum_{n=1}^{\infty} (2n+1) \,\mathrm{Re}(a_n + b_n). \tag{4.4}$$

whereby the a_n and b_n are the BSCs of a scattered plane wave and a is the particle radius[1]. The SCS quantifies how strongly the light scatters on the particle. The extinction cross section is a measure of the total power removed from an incident light beam by a particle, due to both scattering and absorption.

[1] With this definition the cross section is sometimes also referred as efficiency coefficients. Depending on the literature it is also common to have a different prefactor $2\pi/k^2$. The difference being the geometrical cross sections of the particle.

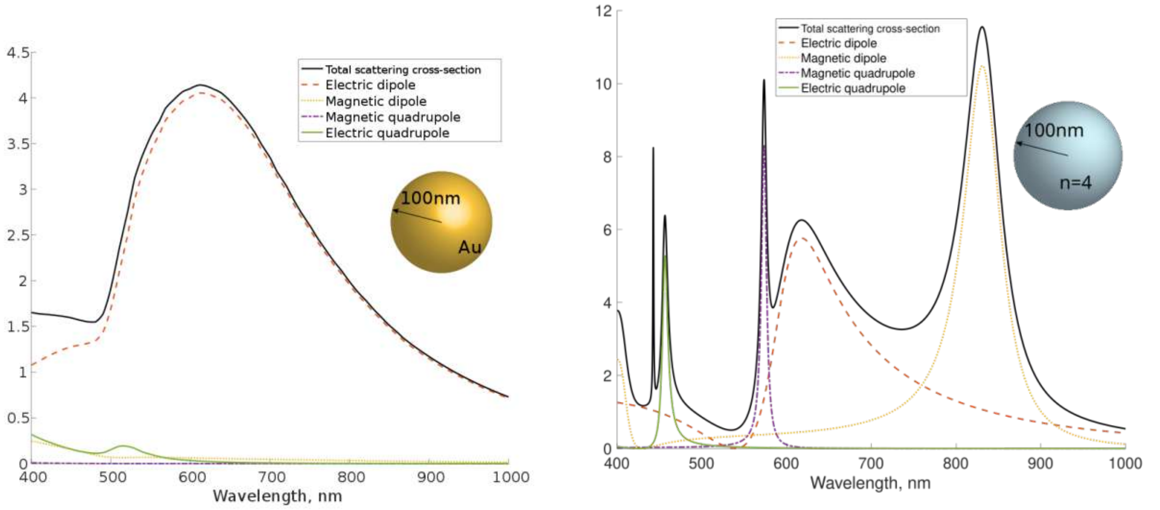

(a) **Gold sphere**
In the case of a gold sphere with radius $r = 100\,\mathrm{nm}$ the scattering cross section over the wavelengths has only one peak (electric dipole).

(b) **Sphere with $n = 4$**
For a sphere with radius $r = 100\,\mathrm{nm}$ and refractive index $n = 4$ the scattering cross section over the wavelengths has many resonance peaks.

Figure 4.1: **Scattering cross section of two different spheres.** The scattering cross section for spherical scatterers is dependent on the wavelength of the incoming light (at least for a certain size). This is due to Mie resonances occurring at certain wavelengths. In our analysis we will focus on those two setups, where we have a scatterer with few resonances and a scatterer with many resonances. The legends for the figures indicates the different poles with different coloured lines and as a black solid line the total SCS.

Figure 4.1 shows the SCS for two different setups taken from [35]. The SCS can be calculated with eq. (4.3), which is also proportional to the power of the scattered part of a plane wave. The a_n and b_n are the BSCs of a scattered plane wave. In the first setup the scatterer is a gold sphere with radius $r = 100\,\mathrm{nm}$. In the second setup the scatterer is a sphere with radius $r = 100\,\mathrm{nm}$ and refractive index $n = 4$ without dispersion. For both setups the scattering cross section for different wavelengths is calculated. In the first setup it can be seen that the cross section has only one peak, which is due to the electric dipole mode. For the second setup with the high refractive index we see that there are many different peaks. This characteristic of the second setup can be quite interesting for the different MISs and how the Fisher information will scale with the different resonances.

4.2 Maximum information states for a spheres with varying wavelength

A higher SCS implies that there is more scattering and with more scattering we generally expect a higher Fisher information. Assuming there is some connection between the Fisher information of the MIS and the scattering cross section, we want to compare those quantities. For that we take one parameter, which we vary and calculate the scattering cross section and the MIS while all the other system parameters stay the same.

We start with optimisations for the same scatterers as in Fig. 4.1, so we can compare our results with known setups.

4.2.1 Setup 1: Gold sphere for different wavelengths

The first setup we look at is the gold sphere. The gold sphere has only one peak in the scattering cross section and in the considered frequency interval (see Fig. 4.1(a)), which makes it easier to analyse. For the optimisation run we start with the wavelength $\lambda_l = 400\,\text{nm}$ and increase it by $\Delta\lambda = 10\,\text{nm}$ up to $\lambda_u = 1000\,\text{nm}$. This requires 61 optimisation runs.

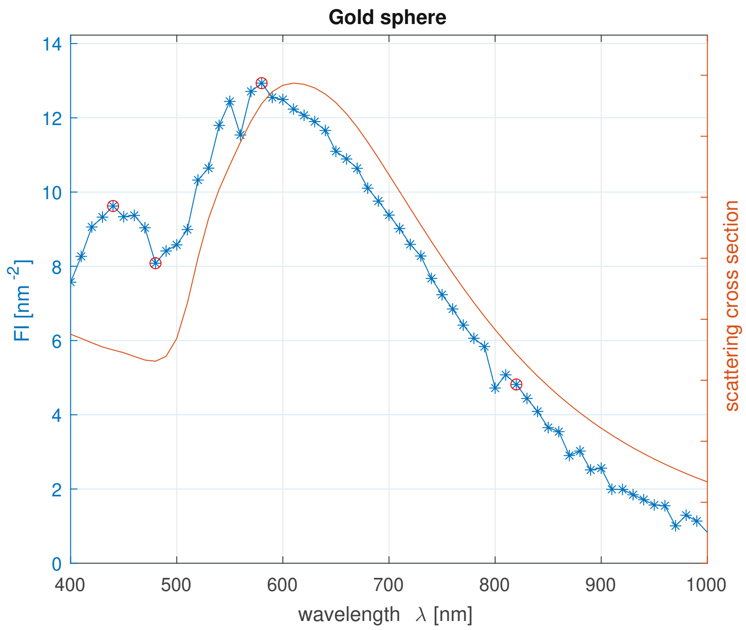

Figure 4.2: **The Fisher information and SCS for a gold sphere.** The blue curve represents the Fisher information on the the camera for the MISs. Each point represents an optimisation run and each point marked with a red circle will be analysed in more detail. The orange curve represents the scattering cross section calculated with eq. (4.3).

Figure 4.2 shows the Fisher information on the camera for the MIS and the scattering cross section as a function of the wavelength. The blue curve represents the Fisher information with each optimisation run marked and the orange curve represents the scattering cross section. The curves show a similar dependency of the wavelength, which is plausible because higher scattering implies that a higher intensity can arrive on the camera. However, there are slight differences between these two curves, further investigations are necessary to understand this behaviour. In appendix D, we look at different types of SCSs, in particular the forward and backward scattering cross sections. Those help to understand the phenomenon of the slightly shifted curves.

In addition, four points are marked red in Fig. 4.2. The MISs corresponding to those points are analysed in more detail. We do this because we want to check whether the beams look the same as the previous results (see sec. 3.2 and 3.3) or deploy a different physical effect to generate the Fisher information.

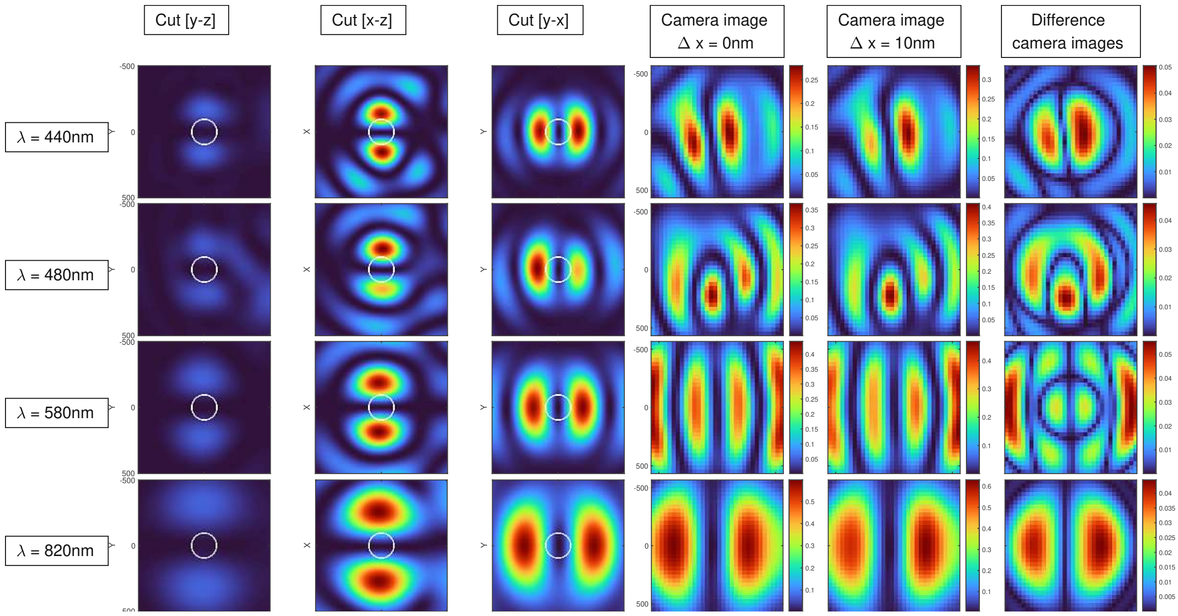

Figure 4.3: **Different MISs for the setup with the gold sphere.** Four MISs for different wavelength. The chosen points are marked as red circles in Fig. 4.2. The first three columns are three different cuts, the fourth and fifth column are the camera images for $\Delta x = 0\,\text{nm}$ and $\Delta x = 10\,\text{nm}$ respectively and the last column is the difference between those two camera images.

Figure 4.3 shows the MISs for four more or less randomly chosen parameter points with a wavelength of $\lambda_1 = 450\,\text{nm}, \lambda_2 = 560\,\text{nm}, \lambda_3 = 620\,\text{nm}$ and $\lambda_4 = 820\,\text{nm}$, respectively (the red marked points in Fig. 4.2). The different MISs have a similar shape even though the Fisher information for these states is quite different. Only a few MISs have a different shape. In appendix F.2.1 is a more detailed view for the beams and additionally some other beams from this optimisation run.

The gold sphere has only one peak in the studied frequency interval of the SCS and the Fisher information for the MISs on the camera has a similar dependence on the wavelength as the SCS. Furthermore, there is no real deviation to the results in chapter 3 in terms of the shape of the MISs. This might be due to the fact that the gold sphere has no sharp Mie resonances. In the following we will look at a setup which has more resonances as the gold sphere.

4.2.2 Setup 2: Sphere with a refractive index of 4 for different wavelengths

The second setup we analyse is the sphere with a refractive index of $n = 4$. The same sphere as was used in Fig. 4.1(b). In contrast to the previously used gold sphere, this sphere has more resonances, which may lead to interesting MISs. The first optimisation run is with $\lambda_l = 400\,\mathrm{nm}$ and for each further optimisation run we increase it by $\Delta\lambda = 10\,\mathrm{nm}$ up to $\lambda_u = 1000\,\mathrm{nm}$. This is the same parameter space as used in the previous section.

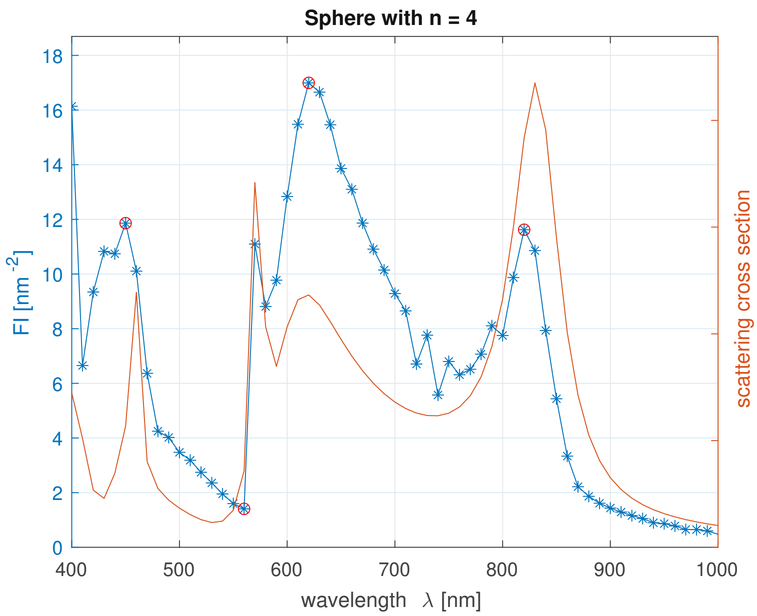

Figure 4.4: **The Fisher information and SCS for a sphere with refractive index of 4.** The blue curve represents the Fisher information on the the camera for the MISs. Each point represents an optimisation run and each point marked with a red circle will be analysed in more detail. The orange curve represents the scattering cross section calculated with eq. (4.3)

Figure 4.4 shows the SCS as the orange curve and the Fisher information for the MISs on the camera as the blue curve. As can be seen there is Fisher information and the SCS have a similar dependency on wavelength. Furthermore, it can be seen that some resonances lead to higher Fisher information, but this is not true for all resonances are to the same degree. This is mostly due to setup specific configurations. In appendix D we will look again at specific cross sections, namely the forward and backward SCS.

The attentive reader may have noticed the missing peak in this figure compared to Fig. 4.1(b). The reason for that is the low resolution for the wavelength, which means that none of our data points coincides with the missing peak. The resolution can be easily enhanced by doing more optimisation runs, but this is quite time consuming procedure. We look at four different MISs for different points in the parameter space, as we did in the previous section. Those points are marked as a red circle in Fig. 4.4.

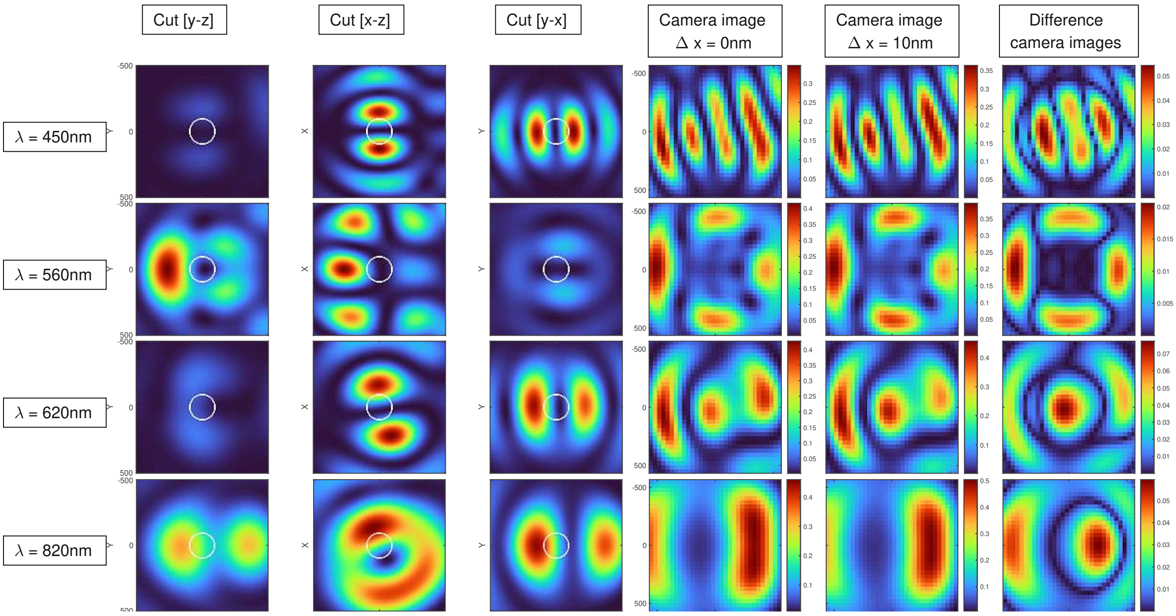

Figure 4.5: **Different MISs for the setup with a sphere with an refractive index of 4.** Four MISs for different wavelength. The chosen points are marked as red circles in Fig. 4.4. The first three columns are three different cuts, the fourth and fifth column are the camera images for $\Delta x = 0\,\mathrm{nm}$ and $\Delta x = 10\,\mathrm{nm}$ respectively and the last column is the difference between those two camera images.

Figure 4.5 shows the MISs for $\lambda_1 = 450\,\mathrm{nm}, \lambda_2 = 560\,\mathrm{nm}, \lambda_3 = 620\,\mathrm{nm}$ and $\lambda_4 = 820\,\mathrm{nm}$. Three of them have a Mie resonance and therefore generate rather high Fisher information. Only λ_2 is at the point without resonance and has a low SCS, which leads to low Fisher information. For this setup we get more different types of MISs. In appendix F.2.2 we show some of the MISs in more detail. The resonances that occur with a scatterer, which has a refractive index, lead to a variety of different shapes for the MISs. We can also observe that the Fisher information has a similar dependence on the wavelength as the SCS, similar to the gold sphere. In the following we will look at a different system parameter and additionally, we will use a different scatterer to see whether the Fisher information will deviate from the SCS.

4.3 Maximum information states for cylinders with varying radii

In the previous section, we have seen that the SCS provide an indication how high the Fisher information is for different parameters. In this section we want to look at a different scatterer and with a different parameter, which we vary. We choose a cylinder as our scatterer and increase the radius.

4.3.1 Setup 3: Gold cylinder with different radii

In the third setup, we work again with a gold scatterer, but here we will use a cylinder and will increase its radius. Starting with a radius of $r_l = 100\,\mathrm{nm}$ and increasing it up to $r_u = 450\,\mathrm{nm}$. For the incoming light we use a wavelength of $\lambda = 488\,\mathrm{nm}$. There are 39 optimisation runs, but those are not uniformly distributed over the wavelength. The reason for that is that we wanted to check a particular region more closely.

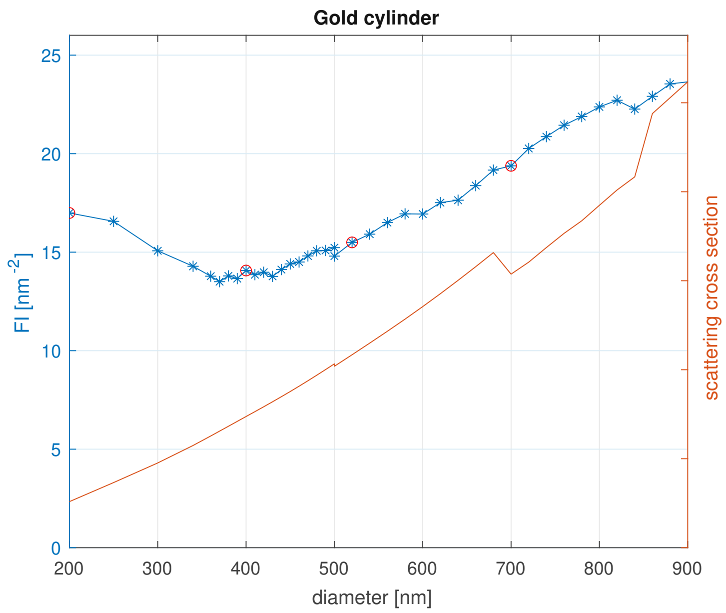

Figure 4.6: **The Fisher information and SCS for a gold cylinder.** The blue curve represents the Fisher information on the the camera for the MISs. Each point represents an optimisation run and each point marked with a red circle will be analysed in more detail. The orange curve represents the scattering cross section calculated with eq. (4.3).

Figure 4.6 shows the SCS in orange, similar to the previous figures, and the Fisher information in blue over the diameter of the cylinder. There are no resonances in the spectrum. The SCS increases with the radius and only between $d \approx 700\,\mathrm{nm}$ and $d \approx 850\,\mathrm{nm}$ there is a difference in the SCS cross section, but this is most likely not due to a physical effect. In this regime, we changed the type of the calculation of the T-matrix, which leads to a slight difference in result. Hence, those results should be studied more closely. In contrast to the SCS the Fisher information for the MISs is declining before it starts to increase again. Interestingly, this happens around $d \approx \lambda$.

As in the previous sections, we marked four points with a red circle and will look at the corresponding MISs.

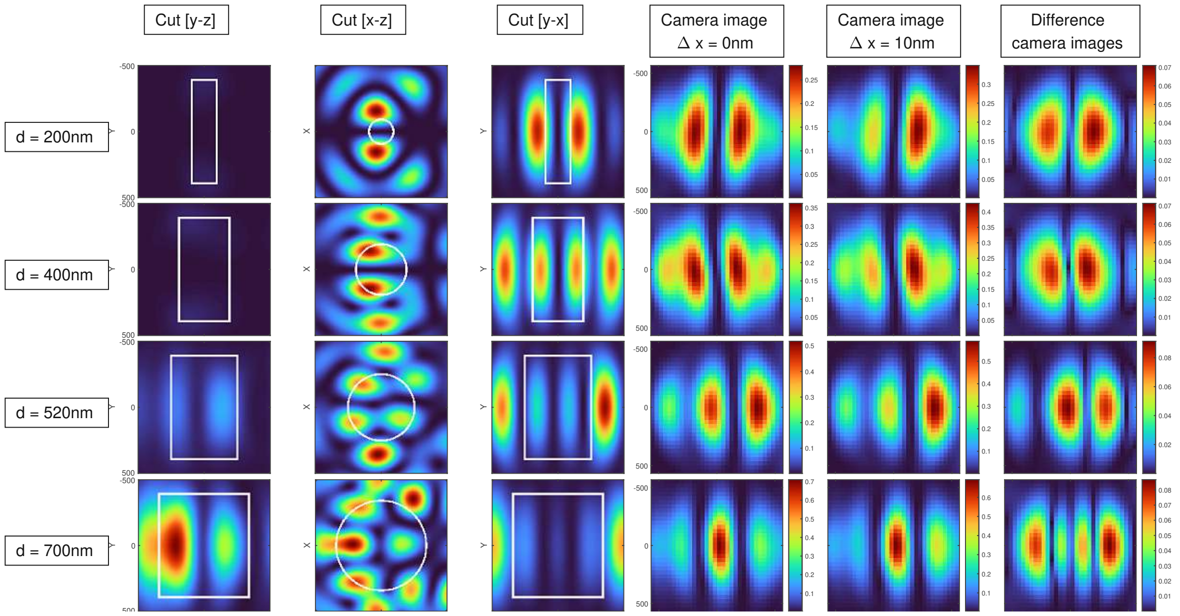

Figure 4.7: **Different MISs for the setup with the gold cylinder.** Four MISs for different wavelength. The chosen points are marked as red circles in Fig.4.2. The first three columns are three different cuts, the fourth and fifth column are the camera images for $\Delta x = 0\,\mathrm{nm}$ and $\Delta x = 10\,\mathrm{nm}$ respectively and the last column is the difference between those two camera images.

Figure 4.7 shows the MISs for the points with a diameter of $d_1 = 200\,\mathrm{nm}$, $d_2 = 400\,\mathrm{nm}$, $d_3 = 520\,\mathrm{nm}$ and $d_4 = 700\,\mathrm{nm}$. The first beam is almost the same as presented in sec. 3.3. Only a few minor parameters are different and therefore the optimisation yields the same type of beam as before. In addition, we also have beams for a target with a bigger diameter. This leads to different types of MISs even tough this setup has no resonances. The reason for that is that the two maxima can not be placed left and right of the target, because the scatterer is too big for this particular wavelength. So the optimisation uses different beams to try to enclose the scatterer, so that a small change in the position leads to a displacement into an intensity maximum. In appendix F.2.3 those MISs are depicted in more detail.

This setup has no resonances and the Fisher information has no peaks. We will look in the following at a setup with a cylinder with a high refractive index. There we will expect to see more resonances as we have seen in sec. 4.2.2.

4.3.2 Setup 4: Cylinder with a refractive index of 4 with different radii

The last setup we look at is a cylinder with a refractive index of 4. With this scatterer we expect again more resonances and therefore also a more peaks in Fisher information as we have seen for the sphere with a refractive index of 4. We start with a cylinder with a radius of $r_l = 100\,\text{nm}$ up to $r_u = 340\,\text{nm}$ with a stepsize of $\Delta r = 10\,\text{nm}$.

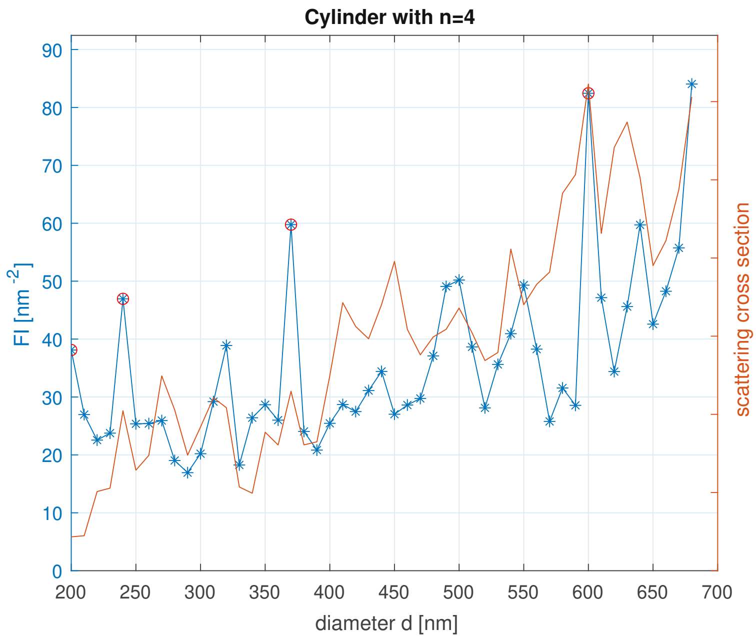

Figure 4.8: **The Fisher information and SCS for a cylinder with refractive index of 4.** The blue curve represents the Fisher information on the the camera for the MISs. Each point represents an optimisation run and each point marked with a red circle will be analysed in more detail. The orange curve represents the scattering cross section calculated with eq. (4.3).

Figure 4.8 shows the SCS in orange and the Fisher information for the MISs on the camera in blue for different diameters. It can be seen that there is more chaotic behaviour than in the previous section, both for SCS and Fisher information. Furthermore, it can be seen that there are few points in the parameter space, which achieve quite a high Fisher information. As we have also seen in the previous section the numerical calculation is not perfect and can lead to some errors. This means that result has to be investigated more in the future. For a better understanding we pick four points, which are marked with a red circle and investigate those in more detail.

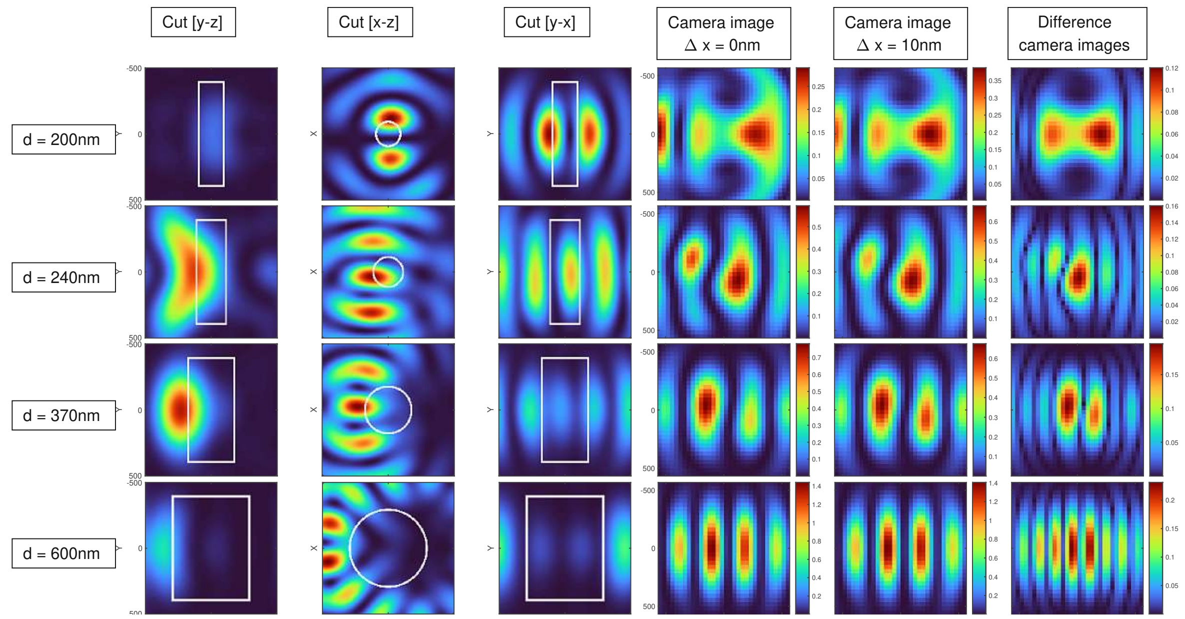

Figure 4.9: **Different MISs for the setup with a cylinder with an refractive index of 4.** Four MISs for different wavelength. The chosen points are marked as red circles in Fig.4.2. The first three columns are three different cuts, the fourth and fifth column are the camera images for $\Delta x = 0\,\text{nm}$ and $\Delta x = 10\,\text{nm}$ respectively and the last column is the difference between those two camera images.

Figure 4.9 shows the MISs for $d_1 = 200\,\text{nm}, d_2 = 240\,\text{nm}, d_3 = 370\,\text{nm}$ and $d_4 = 600\,\text{nm}$. All of them can achieve a relatively high Fisher information. In particular, the beam for the scatterer with d_4 has a high Fisher information and also interesting symmetry. All of them have a unique shape and generate the Fisher information with different physical effects. Nevertheless is the result for this scatterer quite different from those before and needs further investigation to confirm the correctness of the results. In appendix F.2.4 those MISs are depicted in more detail.

4.4 Summary and discussion

In this chapter we looked at four different scatteres and varied the wavelengths and the radii respectively and tracked the Fisher information for the MISs on the camera. Furthermore, we looked at the SCS of the associated scatterer and compared this to the Fisher information. In general we can say that the SCS has a high influence on the Fisher information as expected. Some resonances work better than others for our particular setup, but for other types of setups this might be different.

The MISs for different setups can differ quite a lot and use different types of physical effects to generate the Fisher information on the camera. Nevertheless we see that one type of MIS appears for different types of setups. This MIS was also the result in the previous chapter 3 and has an intensity maximum on the left and right side of the target.

5 Conclusion and Outlook

In this thesis, we have explored the optimisation of incident wavefronts to maximise information retrieval from scattered optical fields. By employing Fisher information as a guiding metric, we developed a computational framework to identify Maximum Information States (MIS) for different scattering setups. Using generalised Lorenz-Mie Theory and the T-matrix method, we accurately modelled light scattering and evaluated the information content captured by a camera. In this thesis we focused on the Fisher information for the lateral position with a camera at a fixed distance away from the origin.

Our results demonstrate that optimally tailored beams can significantly enhance measurement precision compared to conventional beams. Specifically, we applied our method to spherical and cylindrical scatterers, showing a substantial improvement in Fisher information and thus in parameter estimation precision. Additionally, we validated the robustness of our optimisation approach by testing different initial conditions, confirming the consistency of the obtained MIS.

Furthermore, we have shown that the Fisher information on the camera for the MIS has a similar dependency on the setup parameters as the scattering cross section (SCS). This is not surprising, because with more scattering more photons arrive at the camera and thereby increase the Fisher information. A particularly interesting observation is that for some peaks in the SCS (Mie resonances) the Fisher information increases more than for others. The MIS itself has one particular shape, which appears quite often, but especially for points with a Mie resonance the shape can get quite unique.

These findings contribute to the broader field of wavefront shaping and precision optical measurements. The proposed methodology could be extended to more complex scatterers or more experimental constraints, such as the direction of the incoming beam. Future work may explore practical implementations of these optimised beams in experimental setups, as well as their applicability in fields such as biomedical imaging, optical trapping, and nanophotonics.

6 Acknowledgements

I would like to express my sincere gratitude to all those who supported and guided me throughout this journey.

First and foremost, I am deeply thankful to my supervisors, Stefan Rotter and Maximilian Weimar, for their continuous support, expert guidance, and valuable feedback throughout the course of this project. Their encouragement and constructive suggestions greatly enhanced the quality of this work.

Special thanks to group of Nikolay Zheludev for their collaboration, insights and all the fruitful discussions.

I am especially thankful to Une Butaite for generously providing her code and sharing their technical expertise, which played a crucial role in the development of this project.

Finally, I want to thank my family, friends and my girlfriend for their constant motivation, patience, and moral support throughout this endeavour.

A Vector spherical wave functions (VSWF)

We consider the Helmholtz equation in three dimensions for the complex three dimensional vector field $\mathbf{E}(\mathbf{r})$

$$\nabla^2\mathbf{E} + k^2\mathbf{E} = 0 \tag{A.1}$$

The solutions of the vector Helmholtz equation are the VSWF and form a complete orthogonal basis.

$$\mathbf{M}_{nm}^{(1,2)}(kr) = N_n h_n^{(1,2)}(kr)\mathbf{C}_{nm}(\theta,\phi) \tag{A.2}$$

$$\mathbf{N}_{nm}^{(1,2)}(kr) = \frac{h_n^{(1,2)}(kr)}{krN_n}\mathbf{P}_{nm}(\theta,\phi) + N_n\left(h_{n-1}^{(1,2)}(kr) - \frac{nh_n^{(1,2)}(kr)}{kr}\right)\mathbf{B}_{nm}(\theta,\phi) \tag{A.3}$$

with the normalisation constant $N_n = 1/\sqrt{n(n+1)}$, the vector spherical harmonics

$$\mathbf{B}_{nm}(\theta,\phi) = \mathbf{r}\nabla Y_n^m(\theta,\phi), \quad \mathbf{C}_{nm}(\theta,\phi) = \nabla\times(\mathbf{r}Y_n^m(\theta,\phi)), \quad \mathbf{P}_{nm}(\theta,\phi) = \hat{\mathbf{r}}Y_n^m(\theta,\phi), \tag{A.4}$$

and the spherical Hankel functions

$$h_n^{(1)} = j_n + iy_n, \quad h_n^{(2)} = j_n - iy_n. \tag{A.5}$$

The upperindex (1) and (2) indicating two sets of solutions and are the outward-propagating and inward-propagation respectively multipole fields.

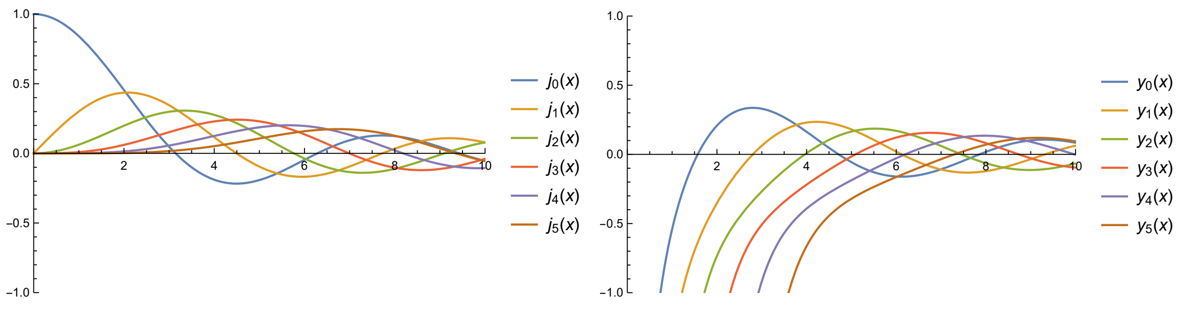

Figure A.1: **Spherical Bessel functions.** The first 6 orders of spherical Bessel functions of the (a) first and (b) second kind.

Figure A.1 shows the spherical Bessel function of the first and second kind. Together the form the spherical Hankel functions from the eq. (A.5). Both of the spherical Hankel functions have a singularity at the origin as can be seen from the figure with spherical Bessel function of the second kind (the imaginary part of the spherical Hankel functions). It is useful to define a third set of solution with no singularity

$$\mathbf{RgM}_{nm}(kr) = \frac{1}{2}\left[\mathbf{M}^{(1)}_{nm}(kr) + \mathbf{M}^{(2)}_{nm}(kr)\right], \tag{A.6a}$$

$$\mathbf{RgN}_{nm}(kr) = \frac{1}{2}\left[\mathbf{N}^{(1)}_{nm}(kr) + \mathbf{N}^{(2)}_{nm}(kr)\right]. \tag{A.6b}$$

Those are the regular vector spherical wavefunctions and we will denote them by the upperindex (3).

The incident beam we can write this with the singularity free multipole field

$$\mathbf{E}_{\text{inc}}(\mathbf{r}) = \sum_{n=1}^{\infty}\sum_{m=-n}^{n} a^{(3)}_{nm}\mathbf{RgM}_{nm}(kr) + b^{(3)}_{nm}\mathbf{RgN}_{nm}(kr). \tag{A.7}$$

Or, alternatively we can write it with the purely incoming wavefunctions

$$\mathbf{E}_{\text{inc}}(\mathbf{r}) = \sum_{n=1}^{\infty}\sum_{m=-n}^{n} a^{(2)}_{nm}\mathbf{M}^{(2)}_{nm}(kr) + b^{(2)}_{nm}\mathbf{N}^{(2)}_{nm}(kr). \tag{A.8}$$

Both of those representations lead to this scattered field

$$\mathbf{E}_{\text{scat}}(\mathbf{r}) = \sum_{n=1}^{\infty}\sum_{m=-n}^{n} p^{(1)}_{nm}\mathbf{M}^{(1)}_{nm}(kr) + q^{(1)}_{nm}\mathbf{N}^{(1)}_{nm}(kr). \tag{A.9}$$

Those two sets are related and with $a^{(3)}_{nm} = 2a^{(2)}_{nm}$ and $b^{(3)}_{nm} = 2b^{(2)}_{nm}$ convertible.

B Fisher information with a Poisson distribution and readout noise

For many real world application, it is necessary to include a read out noise (imperfect measurement of the intensity at a pixel due to thermal fluctuations, electronic noise, etc.) to our poissonian shot noise. This leads to random variable, which is given by

$$Z = X(\theta) + \xi, \tag{B.1}$$

whereby $X(\theta) \sim \text{Pois}(f(\theta))$ and $\xi \sim p_\epsilon(\epsilon)$.

Due to the linearity of the expectation value we can write

$$\mathrm{E}\left[Z\right] = \mathrm{E}\left[X\right] + \mathrm{E}\left[\xi\right] \tag{B.2}$$

The variance of the new random variable can be calculated with

$$\text{Var}(Z) = \text{Var}(X) + \text{Var}(\xi) + 2\text{Cov}(X, \xi) = \text{Var}(X) + \text{Var}(\xi) \tag{B.3}$$

with $\text{Cov}(X, \xi) = 0$, because the random variables are independent from each other.

Because we already know the expectation value and variance for $X(\theta)$, which is $\text{Var}(X(\theta)) = \mathrm{E}\left[X(\theta)\right] = |E_k^{\text{out}}|^2$ we can write

$$\mathrm{E}\left[Z\right] = \left|E_k^{\text{out}}\right|^2 + \mu_\xi \quad \text{and} \quad \text{Var}(Z) = \left|E_k^{\text{out}}\right|^2 + \sigma_\xi^2 \tag{B.4}$$

For the probability distribution of Z, we have to use the convolution of the two probability distributions of X and ξ.

$$p_Z(z) = p_X(x) * p_\xi(\xi) = \int p(x)p(z-x)\,\mathrm{d}x \tag{B.5}$$

In general, it is quite difficult to evaluate that integral[1], therefore, we use in the following different assumptions to calculate the Fisher information.

[1]It should be noted that one of distribution is a discrete distribution and the other one is a continuous distribution. Those two are not compatible with each other. If you want to calculate the distribution of Z, you need to change the normal distribution to a discrete distribution

In addition, we have a joint probability distribution. $p_Z(z)$ gives us the probability distribution for one pixel. For the whole camera image we have to use the product of all probability distributions

$$P_Z(z) = \prod_{k=1}^{N} p_Z(z_k) \tag{B.6}$$

With this product, it is quite difficult to calculate the Fisher information. Therefore is it easier to rewrite the Fisher information for our calculations to

$$\mathcal{I}(\theta) = -\mathrm{E}\left[\left(\partial_\theta^2 \log p(X|\theta)\right)\right], \tag{B.7}$$

since

$$\partial_\theta^2 \log p(X|\theta) = \frac{\partial_\theta^2 p(X|\theta)}{p(X|\theta)} - \left(\frac{\partial_\theta p(X|\theta)}{p(X|\theta)}\right)^2 = \frac{\partial_\theta^2 p(X|\theta)}{p(X|\theta)} - \left(\partial_\theta \log p(X|\theta)\right)^2 \tag{B.8}$$

and

$$\mathrm{E}\left[\frac{\partial_\theta^2 p(X|\theta)}{p(X|\theta)}\right] = \partial_\theta^2 \int p(x|\theta) dx = 0 \tag{B.9}$$

B.1 Case 1: $\xi << |E|^2$

The first case we will look at is with the intensity being much larger than the readout noise. The photon shot noise can be modelled as Poisson distribution and because only a small value is added the distribution $p_Z(z)$ will look similar to the Poisson distribution, which is given by

$$p_Z(z) = \frac{\lambda^{z_k} e^{-\lambda}}{z_k!}. \tag{B.10}$$

Using the expression for the variance in B.4 we can insert $\lambda = \mathrm{E}[Z] = \mathrm{Var}(Z) = |E_k^{\mathrm{out}}|^2 + \sigma_\xi^2$ and furthermore we can calculate the probability distribution for the whole camera image. This leads to

$$P_Z(z) = \prod_{k=1}^{N} \frac{\left(|E_k^{\mathrm{out}}|^2 + \sigma_\xi^2\right)^{z_k} e^{-|E_k^{\mathrm{out}}|^2 + \sigma_\xi^2}}{z_k!}. \tag{B.11}$$

Inserting this into the expression for Fisher information eq. (B.7) yields

$$\mathcal{I}(\theta) = \mathrm{E}\left[\sum_{k=1}^{N} \partial_\theta^2 \left(-z_k \cdot \log\left(\left|E_k^{\mathrm{out}}\right|^2 + \sigma_\xi^2\right) + \left|E_k^{\mathrm{out}}\right|^2 + \sigma_\xi^2 + \log z_k!\right)\right]. \tag{B.12}$$

Taking the derivative with respect to θ twice leads to

$$\mathcal{I}(\theta) = \mathrm{E}\left[\sum_{k=1}^{N} \left(-\frac{\partial_\theta^2 |E_k^{\mathrm{out}}|^2}{|E_k^{\mathrm{out}}|^2 + \sigma_\xi^2} \cdot z_k + \frac{\partial_\theta \left(|E_k^{\mathrm{out}}|^2\right)^2}{\left(|E_k^{\mathrm{out}}|^2 + \sigma_\xi^2\right)^2} \cdot z_k + \partial_\theta^2 \left|E_k^{\mathrm{out}}\right|^2\right)\right]. \tag{B.13}$$

With the expectation value of $\mathrm{E}[z] = |E_k^{\text{out}}|^2 + \sigma_\xi^2$ we get the expression for the Fisher information

$$\mathcal{I}(\theta) = \sum_{k=1}^{N} \left(\frac{\partial_\theta \left(|E_k^{\text{out}}|^2 \right)^2}{|E_k^{\text{out}}|^2 + \sigma_\xi^2} \right) \tag{B.14}$$

B.2 Case 2: $\xi >> |E|^2$

In this case the read out noise of the camera is dominant, which is usually modelled as normal distribution ($\xi \sim N(\mu_\xi, \sigma_\xi^2)$). We then say the distribution of Z has the same shape as the distribution of ξ , but a different expectation value and variance. This leads to

$$p_Z(z|\theta) = N(\mu_z, \sigma_z^2) = \frac{1}{\sqrt{2\pi\sigma_z^2}} \cdot \mathrm{e}^{-\frac{(z-\mu_z)^2}{2\sigma_z^2}}. \tag{B.15}$$

The new expectation value and variance are given by eq. (B.4) and expanding this probability distribution for one pixel to a probability distribution for the camera image yields

$$P_Z(Z|\theta) = \prod_{k=1}^{N} \frac{1}{\sqrt{2\pi \left(|E_k^{\text{out}}|^2 + \sigma_\xi^2 \right)}} \cdot \mathrm{e}^{-\frac{\left(z_k - \left|E_k^{\text{out}}\right|^2 + \mu_\xi\right)^2}{2\left(\left|E_k^{\text{out}}\right|^2 + \sigma_\xi^2\right)}}. \tag{B.16}$$

Inserting this into the expression for Fisher information eq. (B.7) leads to

$$\mathcal{I}(\theta) = -\mathrm{E}\left[\sum_{k=1}^{N} \partial_\theta^2 \left(-\log \sqrt{2\pi \left(|E_k^{\text{out}}|^2 + \sigma_\xi^2 \right)} - \frac{(z_k - |E_k^{\text{out}}|^2 + \mu_\xi)^2}{2\left(|E_k^{\text{out}}|^2 + \sigma_\xi^2 \right)} \right) \right]. \tag{B.17}$$

Taking the derivative with respect to θ twice and calculating the expectation value for $\mathrm{E}[z] = \mu_z$ and $\mathrm{E}[z^2] = \sigma_z^2$ yields this expression for the Fisher information

$$\mathcal{I}(\theta) = \sum_{k=1}^{N} \left(\frac{\partial_\theta \left(|E_k^{\text{out}}|^2 \right)^2}{|E_k^{\text{out}}|^2 + \sigma_\xi^2} + \frac{\partial_\theta \left(|E_k^{\text{out}}|^2 \right)^2}{2\left(|E_k^{\text{out}}|^2 + \sigma_\xi^2 \right)^2} \right) \tag{B.18}$$

B.3 Case 3: $\xi \approx |E|^2$

In this case we can not make assumption or calculation for our joint distribution $p_z(z|\theta)$. Therefore, we have to find a different method of approximating the FI. A way of doing that is to introduce the Linear Fisher information (LFI)

$$J(\theta) = \frac{(\partial_\theta \mu(\theta))^2}{\sigma^2} \tag{B.19}$$

The LFI is a lower bound for the exact Fisher information [36]

$$J(\theta) \leq \mathcal{I}(\theta). \tag{B.20}$$

The two parameters $\mu(\theta)$ and σ^2 are the mean value and the variance respectively. Using the equations in eq. (B.4), we find that

$$J(\theta) = \sum_{k=1}^{N} \frac{\partial_\theta \left(|E_k^{\text{out}}|^2\right)^2}{|E_k^{\text{out}}|^2 + \sigma_\xi^2} \tag{B.21}$$

B.4 Summary

Comparing all three results, we can see that they are quite similar. In fact, for the case 1 and case 3 they are the same. In case 2 we have an additional term, which increases the Fisher information. This is a result because in the normal distribution we have 2 parameters μ_z and σ_z, from which we can gather information. If we would use only the Fisher information from μ_z, we would have the same expression for the Fisher information as in case 1 and case 3.

Nevertheless, we can use the expression from case 1 and case 3 as our Fisher information for all pixel values. The Fisher information in case 2 would be higher than this Fisher information, so we are never cross the limit for the Cramér-Rao bound and all states, which maximises the Fisher information in case 1 and case 3 also maximises the Fisher information in case 2. So in general we can use this expression

$$I(\theta) = \sum_{k=1}^{N} \frac{\partial_\theta \left(|E_k^{\text{out}}|^2\right)^2}{|E_k^{\text{out}}|^2 + \sigma_\xi^2} \tag{B.22}$$

as the final expression. Furthermore, is the additional noise σ_ξ^2 a nice feature, because $|E_k^{\text{out}}|^2$ could be essentially zero for some pixel and would lead to a divergence. The new noise avoids a division by a really small value.

C Maximum information states for different noise

As we did for the case with one pixel we want to investigate whether the function $\bar{f}(x)$ and $\bar{g}(x)$ have the maximum states. The functions are defined with

$$\bar{f}(\mathbf{x}) = \sum_{i=1}^{N} \frac{\partial_\theta(\mathbf{x}_i)^2}{\mathbf{x}_i + \sigma_\xi^2} \quad \text{and} \quad \bar{g}(\mathbf{x}) = \sum_{i=1}^{N} \frac{\partial_\theta(\mathbf{x}_i)^2}{\mathbf{x}_i + \sigma_\xi^2 + \delta\sigma_\xi^2} \tag{C.1}$$

Similar as we have done before we can now construct a function $\bar{h}$, which transforms one of the function into the other one ($\bar{g}(x) = \bar{h}(\bar{f}(x))$). This function is given by

$$\bar{h}(y) = \sum_{i=1}^{N} \frac{y\partial_\theta(\mathbf{x}_i)^2 - \sum_{j=1}^{N} \frac{\partial_\theta(\mathbf{x}_j)^2}{\mathbf{x}_j+\sigma_\xi^2} \partial_\theta(\mathbf{x}_i)^2 \bar{\delta}_{ij}}{\partial_\theta(\mathbf{x}_i)^2 + y\delta\sigma_\xi^2 - \sum_{j=1}^{N} \frac{\partial_\theta(\mathbf{x}_j)^2}{\mathbf{x}_j+\sigma_\xi^2} \delta\sigma_\xi^2 \bar{\delta}_{ij}} \tag{C.2}$$

with

$$\bar{\delta}_{ij} = (1 - \delta_{ij}) = \begin{cases} 1, & i \neq j \\ 0, & i = j \end{cases} \tag{C.3}$$

With this more complicated expression for $\bar{h}(y)$, we can check whether the function is increasing monotonically.

$$\bar{h}(\alpha) < \bar{h}(\beta) \tag{C.4}$$

Inserting for the function $\bar{h}$ yields

$$\sum_{i=1}^{N} \frac{\alpha\partial_\theta(\mathbf{x}_i)^2 - \sum_{j=1}^{N} \frac{\partial_\theta(\mathbf{x}_j)^2}{\mathbf{x}_j+\sigma_\xi^2} \partial_\theta(\mathbf{x}_i)^2 \bar{\delta}_{ij}}{\partial_\theta(\mathbf{x}_i)^2 + \alpha\delta\sigma_\xi^2 - \sum_{j=1}^{N} \frac{\partial_\theta(\mathbf{x}_j)^2}{\mathbf{x}_j+\sigma_\xi^2} \delta\sigma_\xi^2 \bar{\delta}_{ij}} < \sum_{i=1}^{N} \frac{\beta\partial_\theta(\mathbf{x}_i)^2 - \sum_{j=1}^{N} \frac{\partial_\theta(\mathbf{x}_j)^2}{\mathbf{x}_j+\sigma_\xi^2} \partial_\theta(\mathbf{x}_i)^2 \bar{\delta}_{ij}}{\partial_\theta(\mathbf{x}_i)^2 + \beta\delta\sigma_\xi^2 - \sum_{j=1}^{N} \frac{\partial_\theta(\mathbf{x}_j)^2}{\mathbf{x}_j+\sigma_\xi^2} \delta\sigma_\xi^2 \bar{\delta}_{ij}} \tag{C.5}$$

To evaluate this expression we will not look at the whole sum instead we focus on each summand on the left hand side. If all of the summands are smaller than the other ones, the whole sum will be smaller than the other sum($\alpha_i < \beta_i \Rightarrow \sum_i \alpha_i < \sum_i \beta_i$). With that we can evaluate the this expression and we get

$$\alpha \left(\partial_\theta(\mathbf{x}_i)^4 - \sum_{j=1}^{N} \frac{\partial_\theta(\mathbf{x}_j)^4}{\mathbf{x}_j + \sigma_\xi^2} \delta\sigma_\xi^2 \bar{\delta}_{ij} + \sum_{j=1}^{N} \frac{\partial_\theta(\mathbf{x}_j)^2}{\mathbf{x}_j + \sigma_\xi^2} \partial_\theta(\mathbf{x}_i)^2 \delta\sigma_\xi^2 \bar{\delta}_{ij} \right) < \beta \left(\partial_\theta(\mathbf{x}_i)^4 - \sum_{j=1}^{N} \frac{\partial_\theta(\mathbf{x}_j)^4}{\mathbf{x}_j + \sigma_\xi^2} \delta\sigma_\xi^2 \bar{\delta}_{ij} + \sum_{j=1}^{N} \frac{\partial_\theta(\mathbf{x}_j)^2}{\mathbf{x}_j + \sigma_\xi^2} \partial_\theta(\mathbf{x}_i)^2 \delta\sigma_\xi^2 \bar{\delta}_{ij} \right). \quad \text{(C.6)}$$

From this expression we can see that $\alpha < \beta$, but with two constraints. The first constraint we have is given by

$$\partial_\theta(\mathbf{x}_i)^2 + y\delta\sigma_\xi^2 - \sum_{j=1}^{N} \frac{\partial_\theta(\mathbf{x}_j)^2}{\mathbf{x}_j + \sigma_\xi^2} \delta\sigma_\xi^2 \bar{\delta}_{ij} > 0 \quad \text{(C.7)}$$

and the second one is given by

$$\partial_\theta(\mathbf{x}_i)^4 - \sum_{j=1}^{N} \frac{\partial_\theta(\mathbf{x}_j)^4}{\mathbf{x}_j + \sigma_\xi^2} \delta\sigma_\xi^2 \bar{\delta}_{ij} + \sum_{j=1}^{N} \frac{\partial_\theta(\mathbf{x}_j)^2}{\mathbf{x}_j + \sigma_\xi^2} \partial_\theta(\mathbf{x}_i)^2 \delta\sigma_\xi^2 \bar{\delta}_{ij} > 0. \quad \text{(C.8)}$$

If one constraints is not fulfilled the function $\bar{h}(y)$ is not monotonically increasing, which leads to a different maximum input state. If both constraints are not fulfilled the function is again monotonically increasing.

In general we can not state that our constraints are fulfilled. This requires a more detailed analysis, which will be given in a future work.

D Forward and backward scattering cross section

As mentioned earlier there is the possibility to look at different types of SCS. This different SCS are the forward and backward SCS. The scattering anisotropic leads to a different amount of scattering in the forward and backwards direction. This effect is generated due to the different parities of the respective poles. For example the electric dipole and electric quadrupole have opposite parity, which leads that the sum of both of them have a decreased electric field on the one side and a increased electric field on the other side.

The derivation of the respective SCS can be found in [34]. The forward SCS is given by

$$C_{\text{sca}}^{\text{forward}} = \frac{1}{a^2k^2}\left|\sum_{n=1}^{\infty}(2n+1)(a_n+b_n)\right|^2 \tag{D.1}$$

and the backward scattering SCS is given by

$$C_{\text{sca}}^{\text{backward}} = \frac{1}{a^2k^2}\left|\sum_{n=1}^{\infty}(2n+1)(-1)^n(a_n-b_n)\right|^2 \tag{D.2}$$

The forward scattering cross section (CFS) and the backwards scattering cross section (CBS) allows us to investigate and analyse our results further.

In the following, we will look at the different setups with spheres as scatterers. The results are the same as in sec. 4.2. The first scatterer is a gold sphere and the second one is a sphere with a refractive index of $n = 4$.

D.1 Setup 1

Starting with the gold sphere for different wavelength, we can calculate the different SCS.

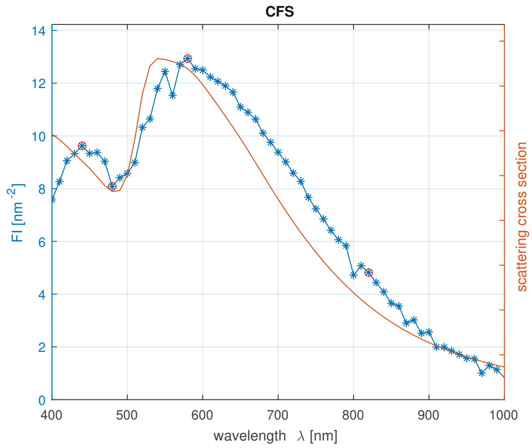

(a) **Forward scattering**
The forward SCS calculated with eq. (D.1) in orange and Fisher information of the MISs on the camera in blue for different wavelengths.

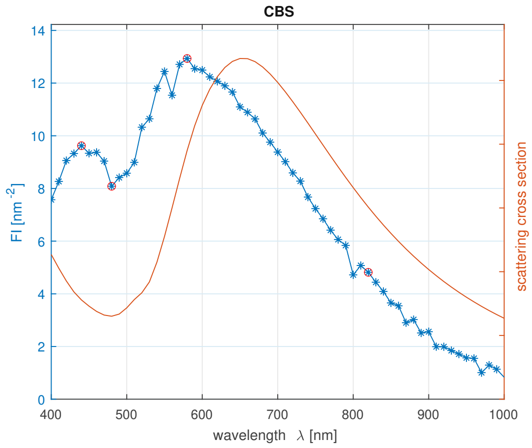

(b) **Backward scattering**
The backward SCS calculated with eq. (D.2) in orange and Fisher information of the MISs on the camera in blue for different wavelengths.

Figure D.1: **Difference in the forward and backward scattering.** Both of the SCSs for a gold sphere are depicted. In (a) there is the forward SCS and in (b) the backward SCS in orange for different wavelength. To compare that to our results the Fisher information on the camera for the different MISs is in blue depicted.

Figure D.1 shows (a) the forward and (b) the backward SCS in orange and the Fisher information of our MISs on the camera in blue. It can be seen that the CFS covers the Fisher information better than the CBS. This phenomenon is quite interesting because we never had a constraint for the direction of the incoming beam and only specified the placement of our camera. Therefore, a setup with a high CBS can also work, and the beam would come from the side, where the camera is placed. This might not be possible in an experiment, but for our simulation, it is a quite interesting phenomenon.

D.2 Setup 2

The same can be done for the sphere with a refractive index of $n = 4$ over different wavelengths.

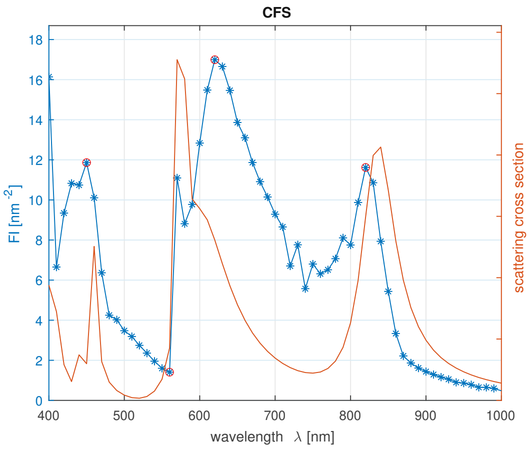

(a) **Forward scattering**
The forward SCS calculated with eq. (D.1) in orange and Fisher information of the MISs on the camera in blue for different wavelengths.

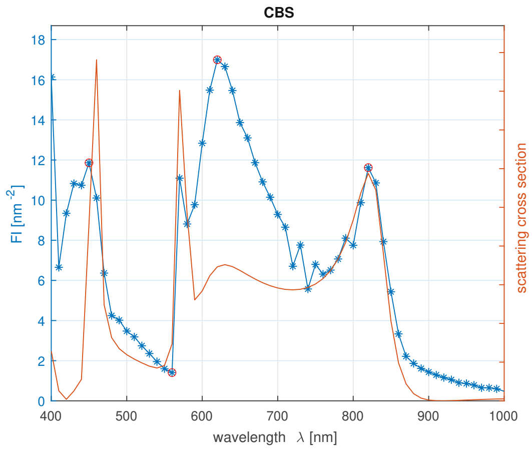

(b) **Backward scattering**
The backward SCS calculated with eq. (D.2) in orange and Fisher information of the MISs on the camera in blue for different wavelengths.

Figure D.2: **Difference in the forward and backward scattering.** Both of the SCSs for a sphere with a refractive indes of $n = 4$ are depicted. In (a) there is the forward SCS and in (b) the backward SCS in orange for different wavelength. To compare that to our results the Fisher information on the camera for the different MISs is in blue depicted.

Figure D.2 shows the forward and the backward SCS in orange and the Fisher information of our MISs on the camera in blue. Similar to the previous setup, we see that some of the peaks are better covered by CFS, but in some other cases it seems that the CBS is covering the Fisher information slightly better.

E Code

All the theories for solving the scattering presented in the chapter 2 require numerical methods and to perform the calculations we used MATLAB with the optical tweezer toolbox (OTT) [12] and OTSLM toolbox for Structured Light Methods [31]. We got inspiration from the work [32] and the author of this work kindly provided her code for us. Part of our code is similar to the code from that work.

As mentioned previously, most optimisation runs were done on the Vienna Scientific Cluster (VSC), which has 128 available cores.However, we encountered the problem that when using all 128 cores, the gradient calculation inside *fmincon* yields wrong results, hence we used only 64 cores.

All results for every optimisation done within the scope of this thesis are saved. The most important result of the optimisation is the BSCs a and b, with those we can construct our beam. The other variables used for the optimisations are also saved as a Matlab object called struct and summarised in the following tables.

E.1 Setup parameters

In the struct parameter are all the necessary values for the setup and presented in the tab. E.1.

Name	Description	Default value
wavelength0	The wavelength of the field in vacuum	488 nm
n_particle	The refractive index of the particle	-
n_medium	The refractive index of the medium	1
dr	The stepsize for the numerical derivative (sec.2.2.2)	6.055×10^{-6}
direction	The parameter θ in the Fisher information*	x
pixels	Number of pixels per axis	32 & 100
distance	The distance from the origin to the camera	500 nm
CameraLength	The length of the camera	1133 nm
Background_Noise	The background noise of a camera σ_ξ^2 (sec.3.2.2)	0.095
fieldtype	The type of calculation**	'regular'
scatter.radius	The radius of the scatterer***	100 nm
scatter.height	The height of the scatterer***	800 nm
wavelength_medium	The wavelength of the light in the medium	$\lambda_m = \lambda/n_m$
nmax	The number of multipole used (sec.2.1.1)	-

Table E.1: **Overview of the setup parameters.** All of this parameters are saved in *struct*, which is called *parameter*. To access a parameter, you have to type "parameter.*name*".

* In general it is possible to use a parameter other than a direction in the Fisher information, but in the code it is only possible to translate and rotate.

** There are two valid options available. The first one is the Option "regular", whereby the fields are calculated as explained in sec. 2.1 and second options is "farfield", whereby a farfield approximation is used. The second option is useful if the camera is far away from the scatterer.

*** In this thesis, we look only at spheres and cylinders as scatterers. The height parameter is only necessary for the cylinder.

E.2 Optimisation parameters

In the struct OptimizerOptions are the parameters for the optimiser.

Name	Description	Default value
MaxIterations	Maximum amount of iteration allowed*	250
constrTol	Tolerance on the constraint violation**	0.1
optimlTol	Termination tolerance on the first-order optimality **	≈ 0
stepTol	Termination tolerance on x**	≈ 0

Table E.2: **Overview of the optimisation parameters.** All of this parameters are saved in *struct*, which is called *OptimizerOptions*. To access a parameter, you have to type "OptimizerOptions.*name*".

* In this thesis we mostly used a maximum iteration to terminate the optimisation procedure.

** For more information see [37]

E.3 Results from the optimiser

In the struct output are the results, which are collected during the optimisation process as well as the final result of the optimisation.

Name	Description
iterations	The amount of iteration done
funcCount	The amount of calls for the optimised function
constrviolation	The constrain violation
stepsize	The stepsize of the optimiser
algorithm	Different algorithm of *fmincon* are possible (Only used *interior-point*).
firstorderopt	Measure of first-order optimality
cgiterations	Total number of Preconditioned Conjugate Gradient (PCG) iterations
message	Short exit message from the optimiser
bestfeasible	Best possible input state found
VariableHistory	The different input states over the iterations
FncHistory	The value of the function over the iterations

Table E.3: **Overview of the results.** All of this parameters are saved in *struct*, which is called *output*. To access a parameter, you have to type "output.*name*".

Most of those results are directly produced by the optimiser itself. Only *VariableHistory* and *FncHistory* are added to the output of the optimiser. For more information on those variables see [37].

F Maximum information beams

In this chapter we will present different the MIS for different kinds of setup.

F.1 Different initial conditions

As explained in the sec. 3.2.1 we did 50 optimisation runs with the exactly the same setup. With that we can see that the optimisation always finds the same maximum of the Fisher information, but there can be a degenerate state. For our two setups we can see that we always find the same(-ish) beam.

F.1.1 Sphere gold

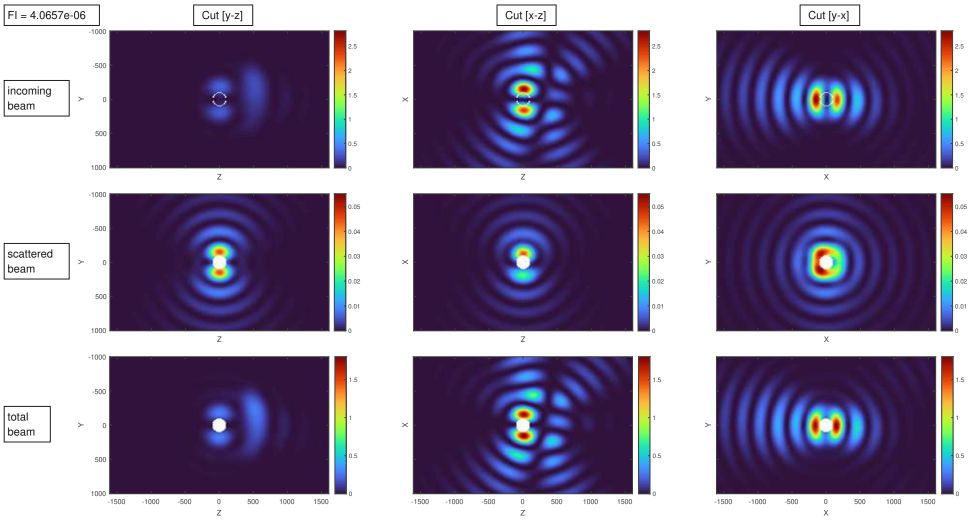

Figure F.1: **Various plots for a MIS.** The three different column represents cuts [y-z], [x-z] and [y-x] respectively. The first row is the MIS for a gold sphere with no scattering, but the scatterer is shown as a thin outline. Second row shows the scattered part of the beam and the third row is the total beam.

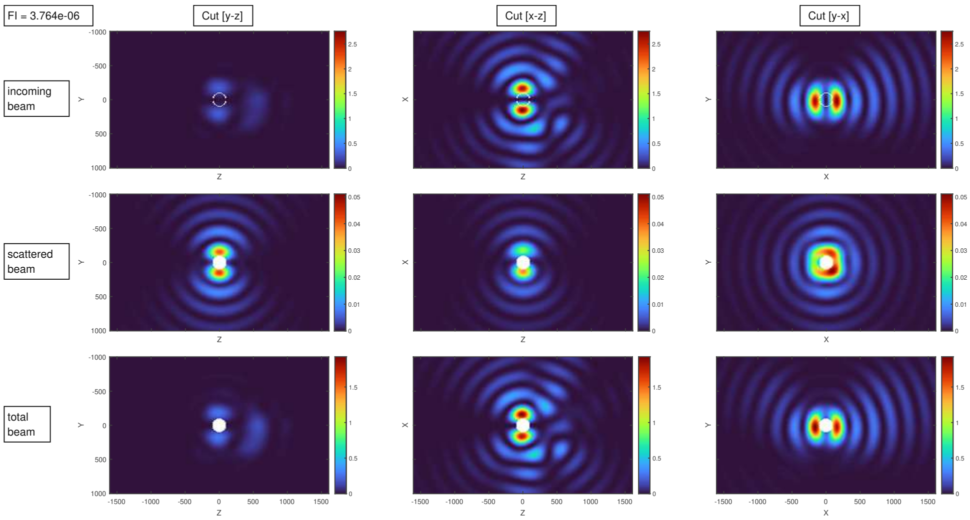

Figure F.2: **Various plots for a MIS.** The three different column represents cuts [y-z], [x-z] and [y-x] respectively. The first row is the MIS for a gold sphere with no scattering, but the scatterer is shown as a thin outline. Second row shows the scattered part of the beam and the third row is the total beam.

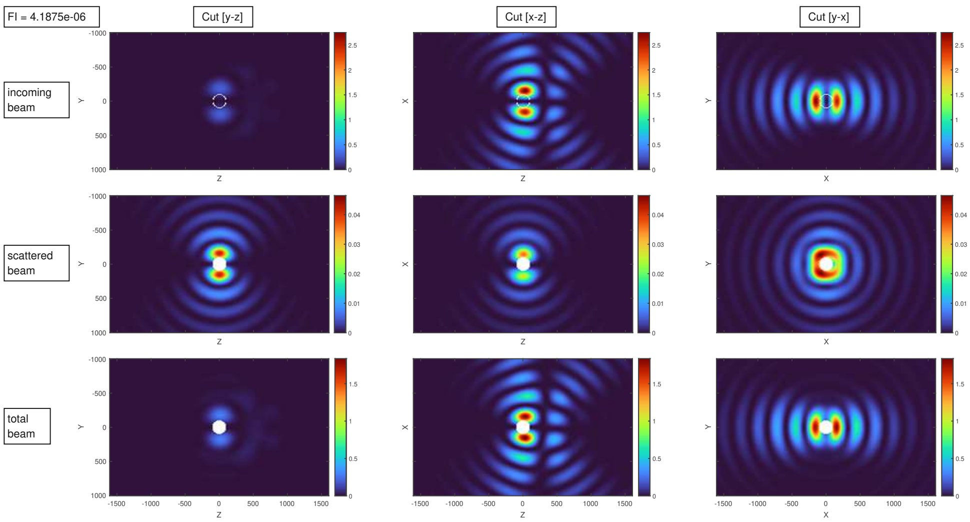

Figure F.3: **Various plots for a MIS.** The three different column represents cuts [y-z], [x-z] and [y-x] respectively. The first row is the MIS for a gold sphere with no scattering, but the scatterer is shown as a thin outline. Second row shows the scattered part of the beam and the third row is the total beam.

F.1.2 Sphere n=4

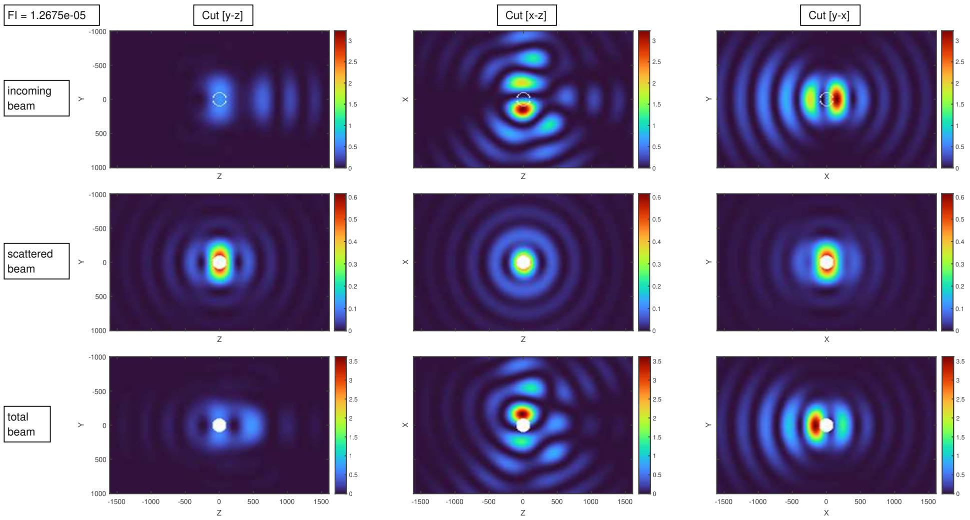

Figure F.4: **Various plots for a MIS.** The three different column represents cuts [y-z], [x-z] and [y-x] respectively. The first row is the MIS for a sphere ($n = 4$) with no scattering, but the scatterer is shown as a thin outline. Second row shows the scattered part of the beam and the third row is the total beam.

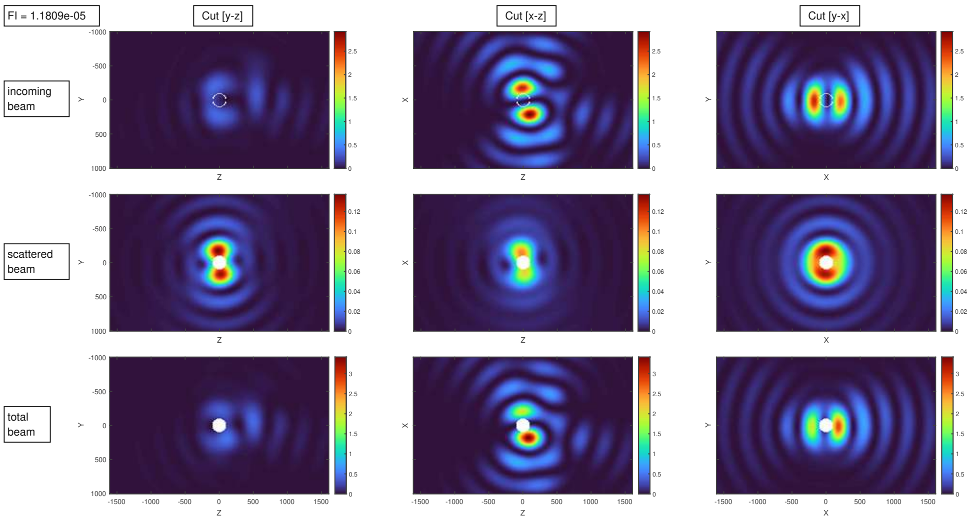

Figure F.5: **Various plots for a MIS.** The three different column represents cuts [y-z], [x-z] and [y-x] respectively. The first row is the MIS for a sphere ($n = 4$) with no scattering, but the scatterer is shown as a thin outline. Second row shows the scattered part of the beam and the third row is the total beam.

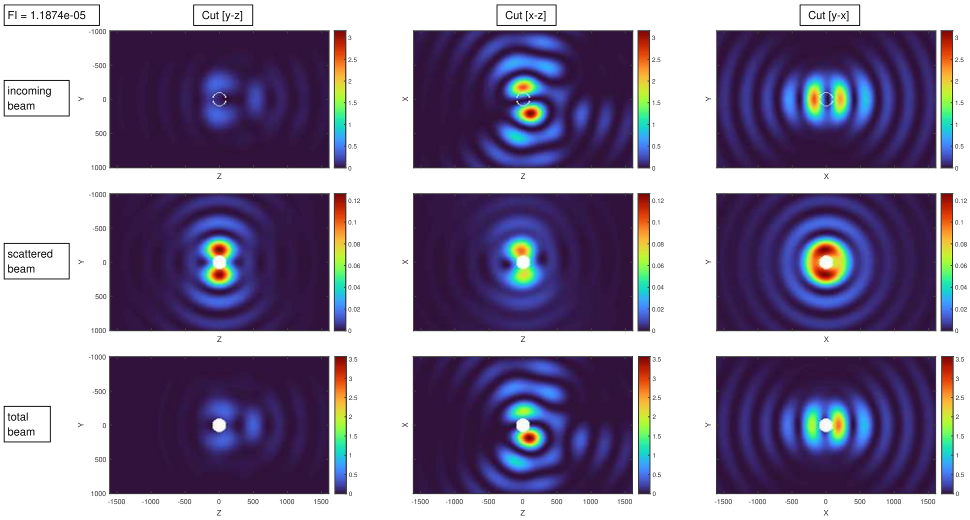

Figure F.6: **Various plots for a MIS.** The three different column represents cuts [y-z], [x-z] and [y-x] respectively. The first row is the MIS for a sphere ($n = 4$) with no scattering, but the scatterer is shown as a thin outline. Second row shows the scattered part of the beam and the third row is the total beam.

F.2 Detailed view for MISs for different parameters

In chapter 4 we introduced four different setups. Here we will present some of those MISs in more detail.

The first setup has a gold sphere as a target and we increase the wavelength of the incoming field to calculate the different MISs. Most of the MISs have the same shape, but there exceptions.

The second setup has a sphere with a refractive index of $n = 4$ as a target and we increase the wavelength of the incoming field to calculate the different MISs. There are appearing more interesting shapes.

The third setup has a gold cylinder as a target and we increase the radius of the scatterer to calculate the different MISs. The MISs have quite different shapes

The fourth setup has a cylinder with a refractive index of $n = 4$ as a target and we increase the radius of the scatterer to calculate the different MISs. With this setup there also a lot of different MISs.

F.2.1 Setup 1: Gold sphere with different wavelengths

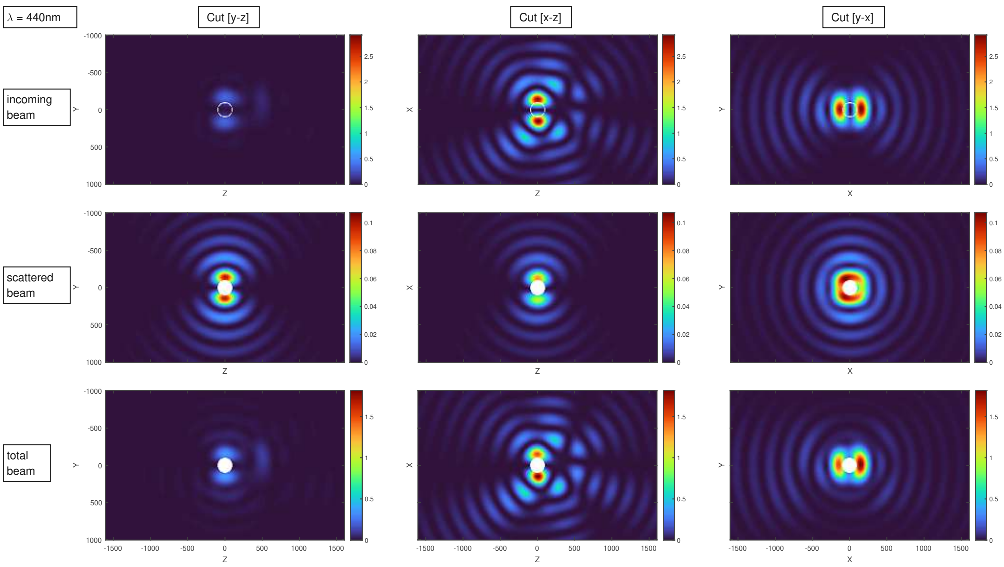

Figure F.7: **Various plots for a MIS.** The three different column represents cuts [y-z], [x-z] and [y-x] respectively. The first row is the MIS for a gold sphere and $\lambda = 440\,\text{nm}$ with no scattering, but the scatterer is shown as a thin outline. Second row shows the scattered part of the beam and the third row is the total beam.

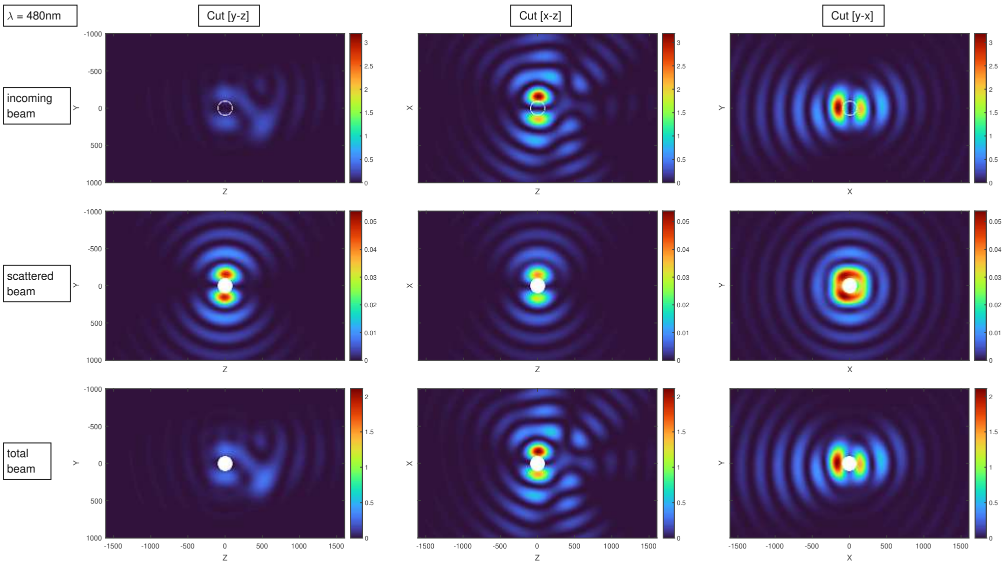

Figure F.8: **Various plots for a MIS.** The three different column represents cuts [y-z], [x-z] and [y-x] respectively. The first row is the MIS for a gold sphere and $\lambda = 480\,\mathrm{nm}$ with no scattering, but the scatterer is shown as a thin outline. Second row shows the scattered part of the beam and the third row is the total beam.

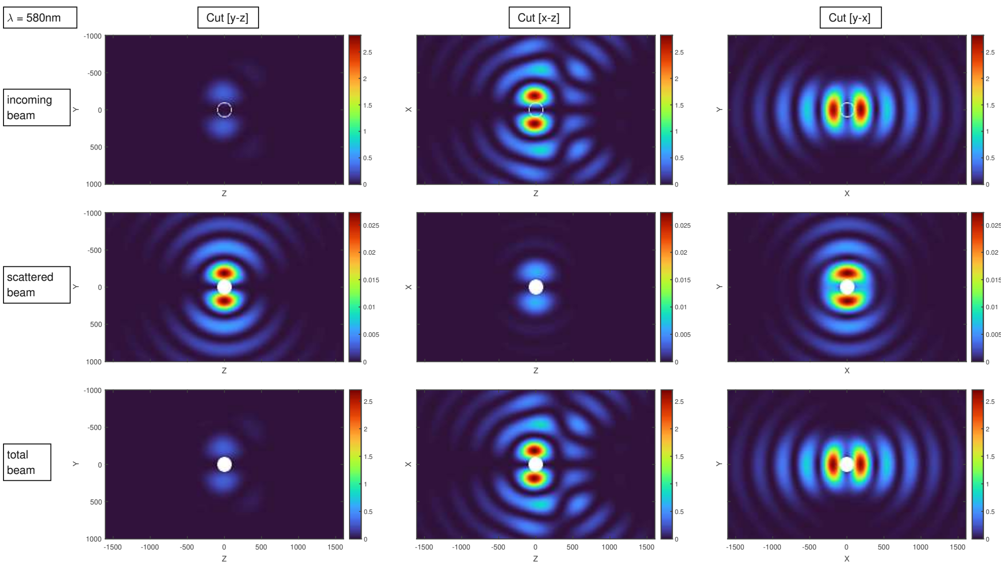

Figure F.9: **Various plots for a MIS.** The three different column represents cuts [y-z], [x-z] and [y-x] respectively. The first row is the MIS for a gold sphere and $\lambda = 580\,\mathrm{nm}$ with no scattering, but the scatterer is shown as a thin outline. Second row shows the scattered part of the beam and the third row is the total beam.

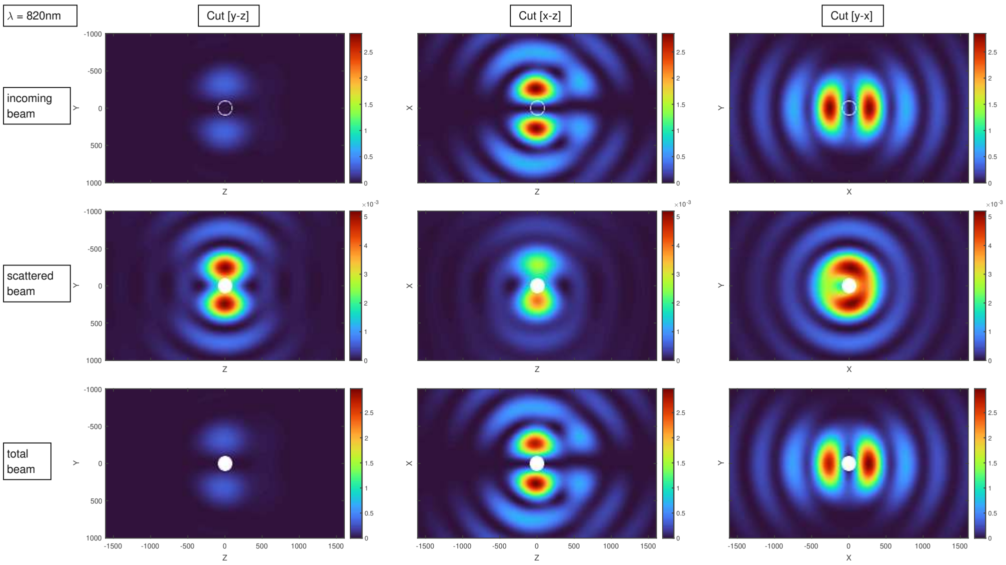

Figure F.10: **Various plots for a MIS.** The three different column represents cuts [y-z], [x-z] and [y-x] respectively. The first row is the MIS for a gold sphere and $\lambda = 820\,\mathrm{nm}$ with no scattering, but the scatterer is shown as a thin outline. Second row shows the scattered part of the beam and the third row is the total beam.

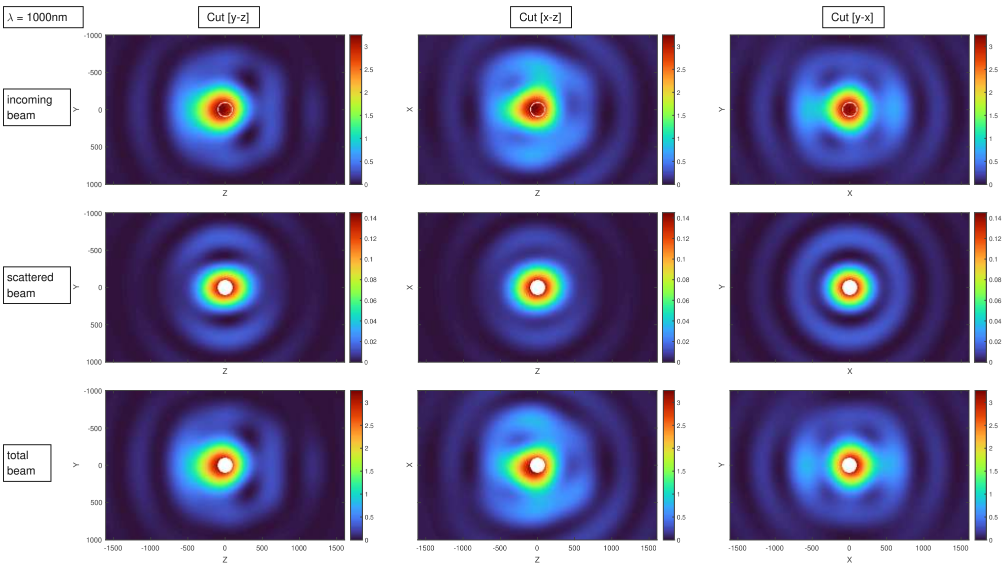

Figure F.11: **Various plots for a MIS.** The three different column represents cuts [y-z], [x-z] and [y-x] respectively. The first row is the MIS for a gold sphere and $\lambda = 1000\,\mathrm{nm}$ with no scattering, but the scatterer is shown as a thin outline. Second row shows the scattered part of the beam and the third row is the total beam.

F.2.2 Setup 2: Sphere with n = 4 and different wavelength

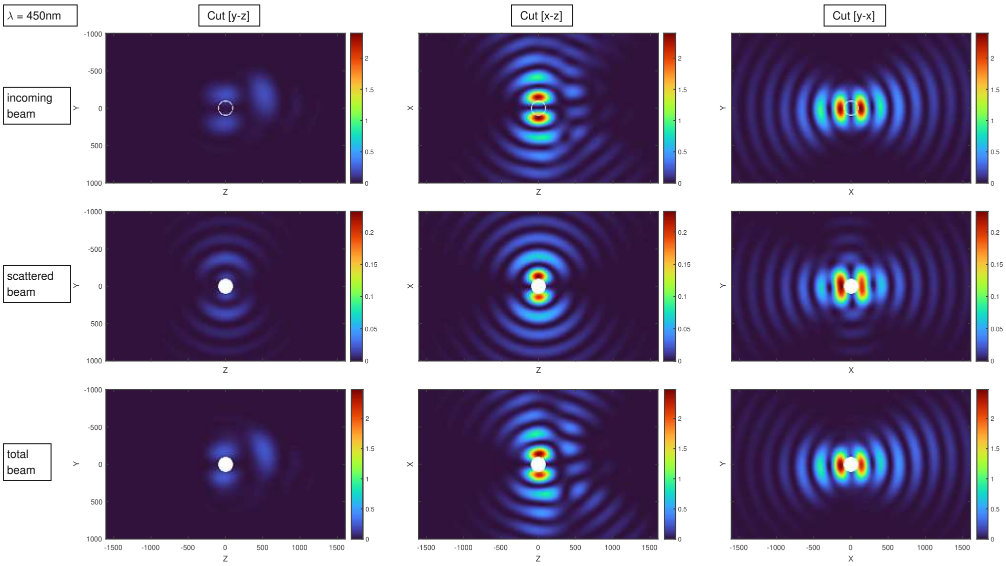

Figure F.12: **Various plots for a MIS.** The three different column represents cuts [y-z], [x-z] and [y-x] respectively. The first row is the MIS for a sphere ($n = 4$) and $\lambda = 450\,\mathrm{nm}$ with no scattering, but the scatterer is shown as a thin outline. Second row shows the scattered part of the beam and the third row is the total beam.

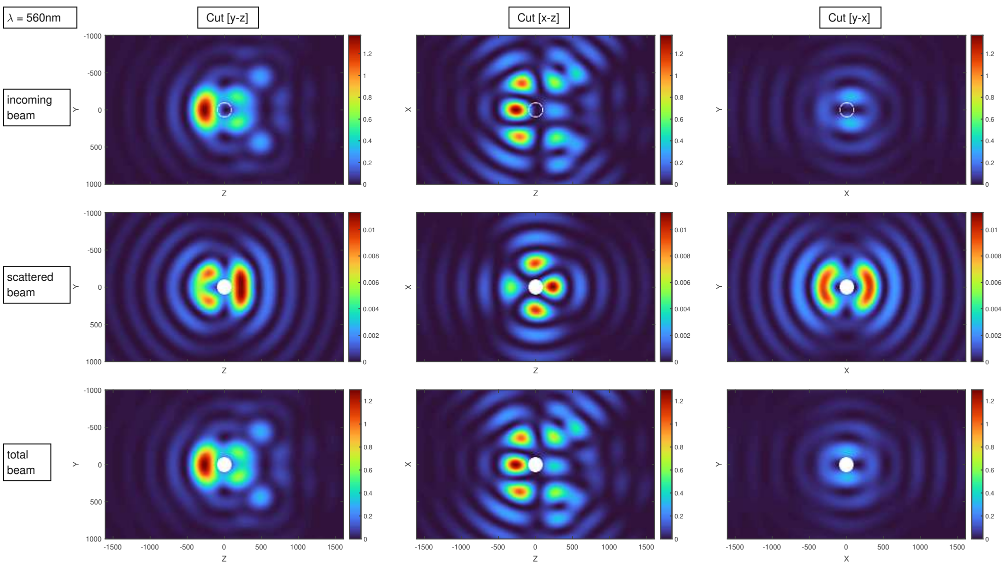

Figure F.13: **Various plots for a MIS.** The three different column represents cuts [y-z], [x-z] and [y-x] respectively. The first row is the MIS for a sphere ($n = 4$) and $\lambda = 560\,\mathrm{nm}$ with no scattering, but the scatterer is shown as a thin outline. Second row shows the scattered part of the beam and the third row is the total beam.

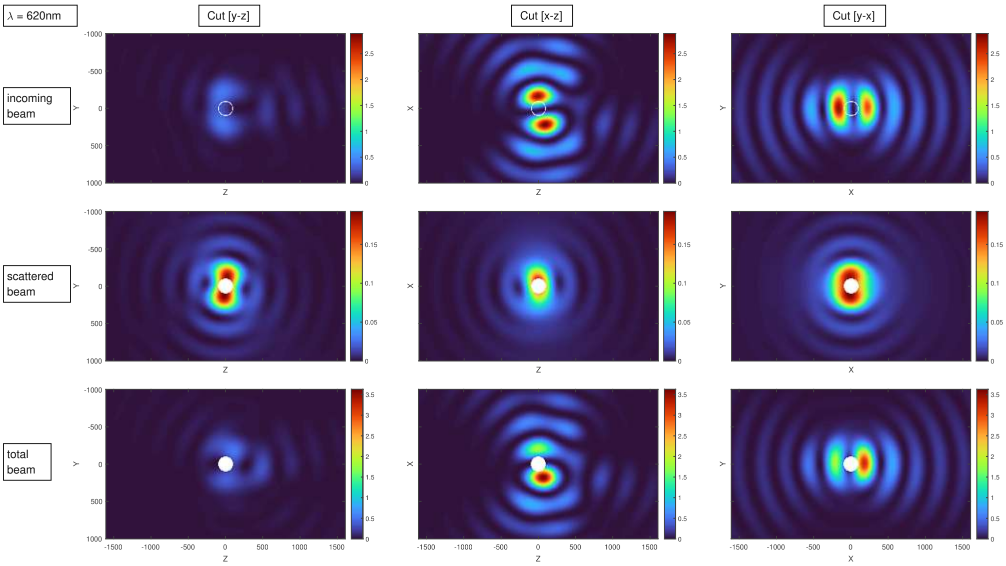

Figure F.14: **Various plots for a MIS.** The three different column represents cuts [y-z], [x-z] and [y-x] respectively. The first row is the MIS for a sphere ($n = 4$) and $\lambda = 620\,\mathrm{nm}$ with no scattering, but the scatterer is shown as a thin outline. Second row shows the scattered part of the beam and the third row is the total beam.

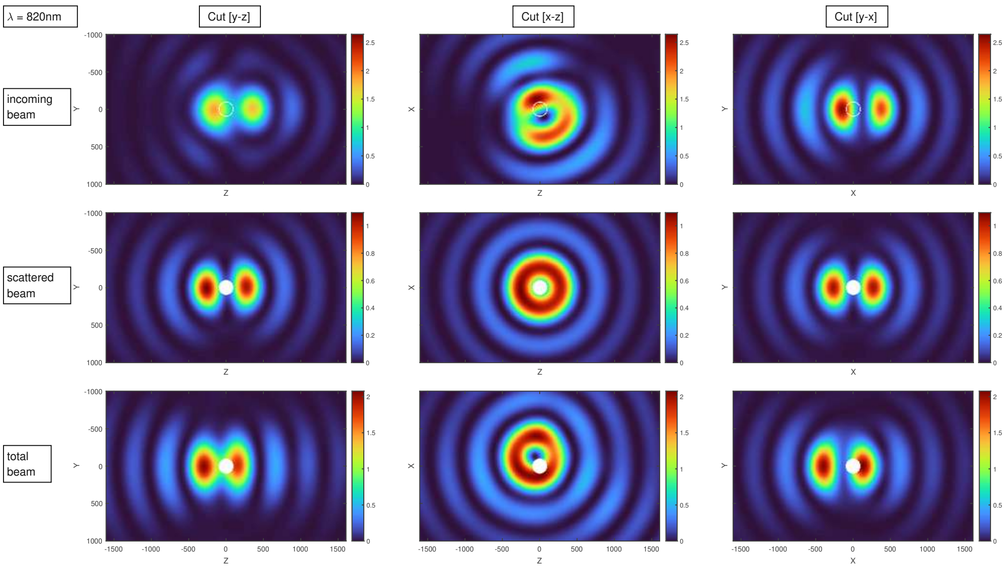

Figure F.15: **Various plots for a MIS.** The three different column represents cuts [y-z], [x-z] and [y-x] respectively. The first row is the MIS for a sphere ($n = 4$) and $\lambda = 820\,\mathrm{nm}$ with no scattering, but the scatterer is shown as a thin outline. Second row shows the scattered part of the beam and the third row is the total beam.

F.2.3 Setup 3: Gold cylinder and different radii

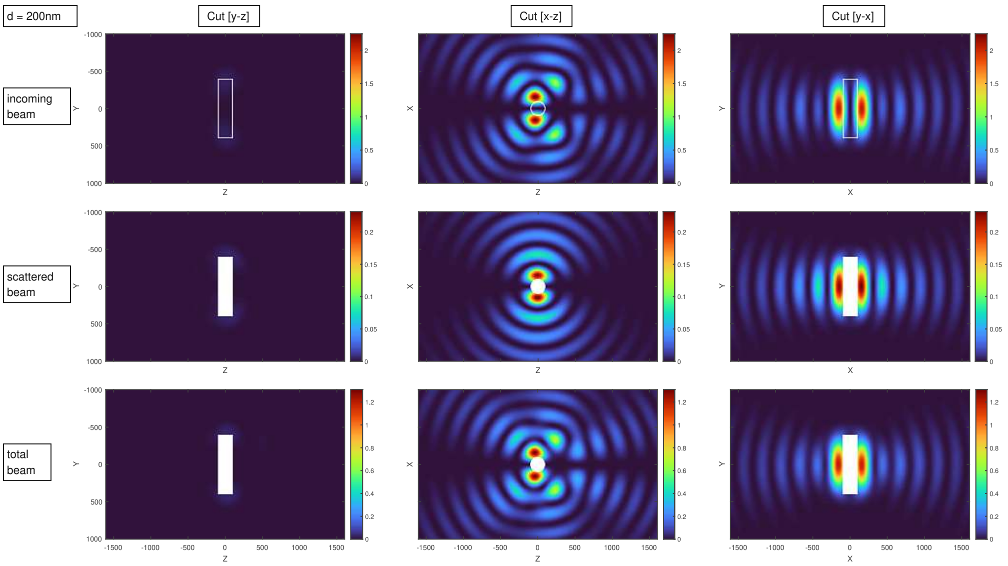

Figure F.16: **Various plots for a MIS.** The three different column represents cuts [y-z], [x-z] and [y-x] respectively. The first row is the MIS for a gold cylinder and $d = 200\,\mathrm{nm}$ with no scattering, but the scatterer is shown as a thin outline. Second row shows the scattered part of the beam and the third row is the total beam.

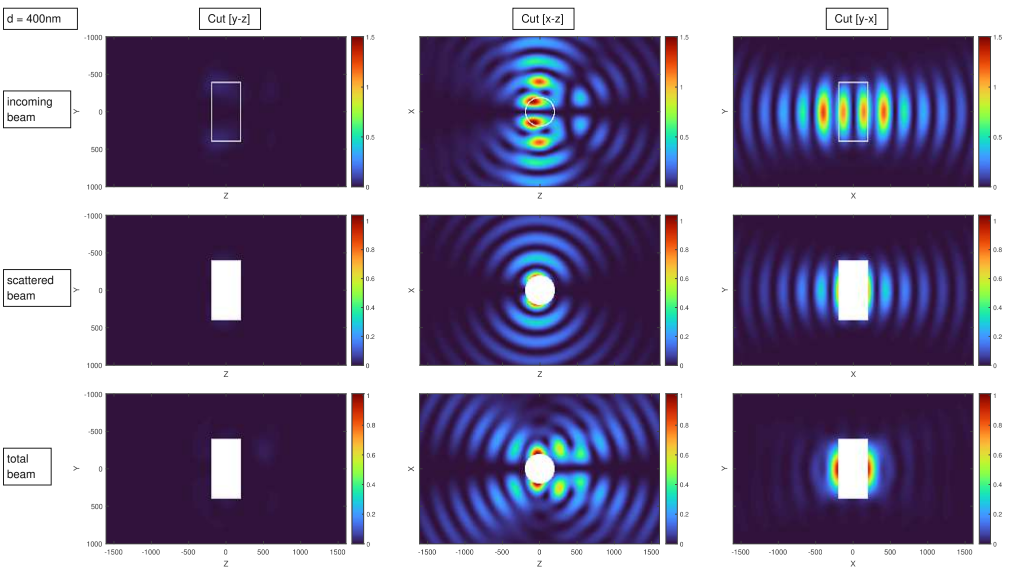

Figure F.17: **Various plots for a MIS.** The three different column represents cuts [y-z], [x-z] and [y-x] respectively. The first row is the MIS for a gold cylinder and $d = 400\,\mathrm{nm}$ with no scattering, but the scatterer is shown as a thin outline. Second row shows the scattered part of the beam and the third row is the total beam.

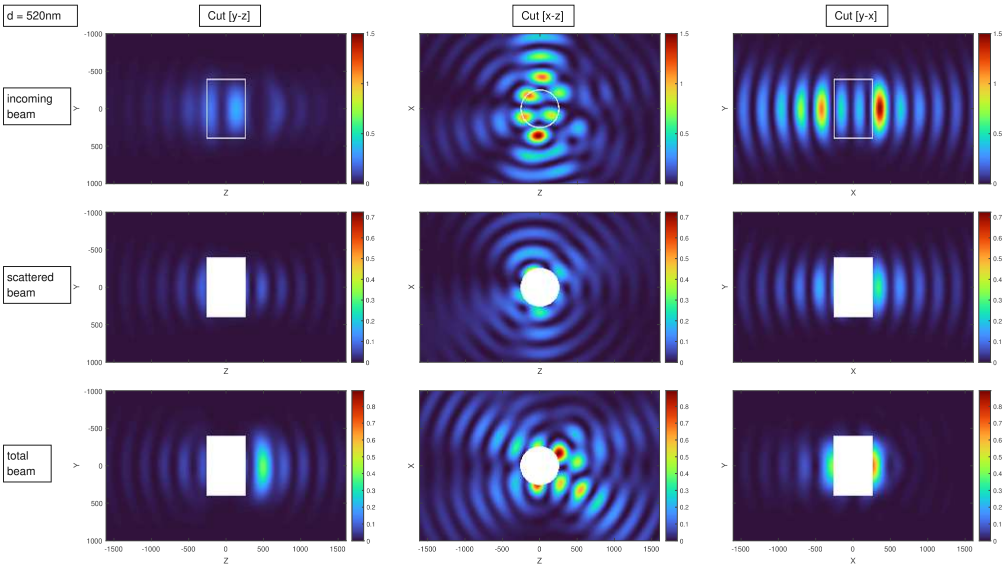

Figure F.18: **Various plots for a MIS.** The three different column represents cuts [y-z], [x-z] and [y-x] respectively. The first row is the MIS for a gold cylinder and $d = 520\,\mathrm{nm}$ with no scattering, but the scatterer is shown as a thin outline. Second row shows the scattered part of the beam and the third row is the total beam.

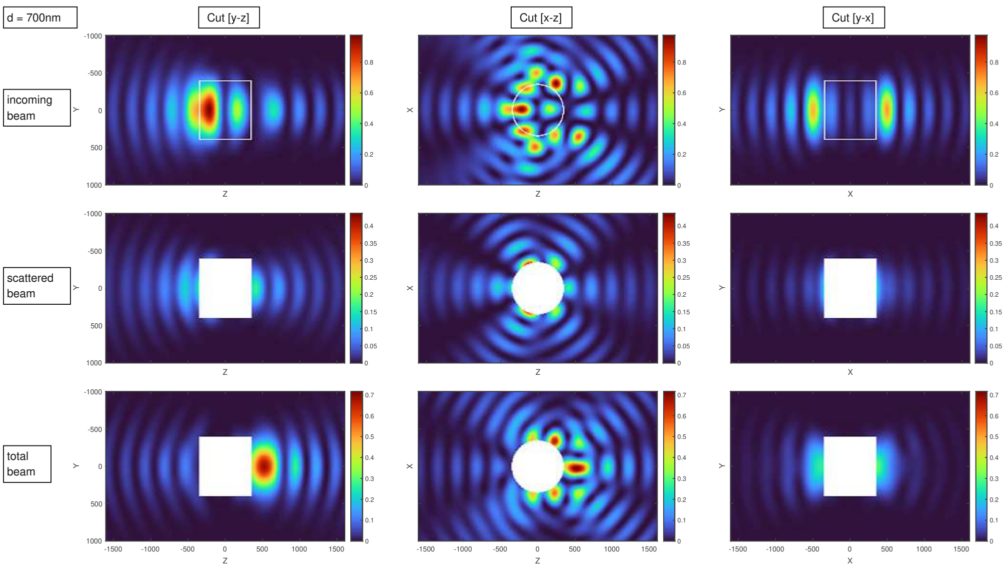

Figure F.19: **Various plots for a MIS.** The three different column represents cuts [y-z], [x-z] and [y-x] respectively. The first row is the MIS for a gold cylinder and $d = 700\,\mathrm{nm}$ with no scattering, but the scatterer is shown as a thin outline. Second row shows the scattered part of the beam and the third row is the total beam.

F.2.4 Setup 4: cylinder with n = 4 and different radii

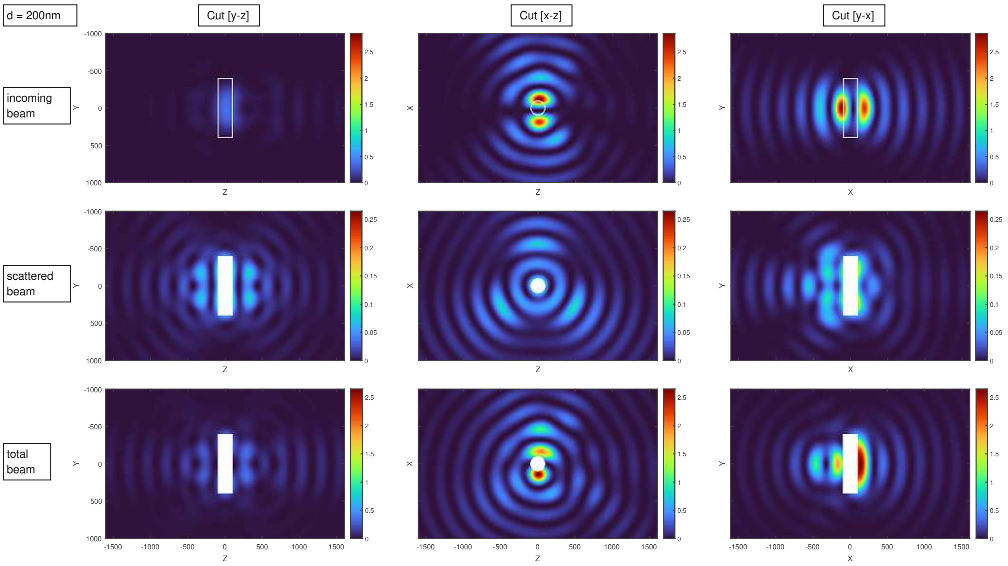

Figure F.20: **Various plots for a MIS.** The three different column represents cuts [y-z], [x-z] and [y-x] respectively. The first row is the MIS for a cylinder ($n = 4$) and $d = 200\,\mathrm{nm}$ with no scattering, but the scatterer is shown as a thin outline. Second row shows the scattered part of the beam and the third row is the total beam.

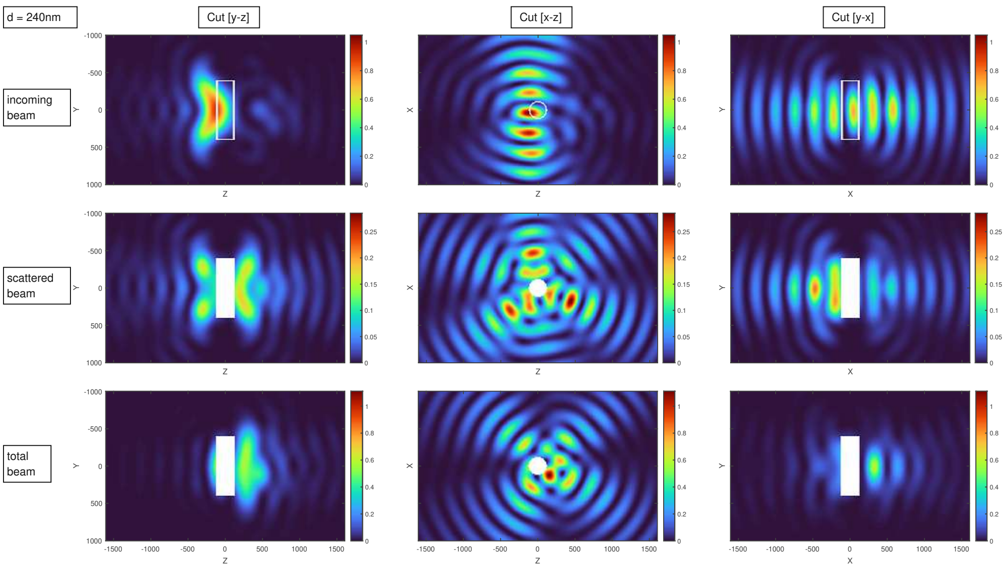

Figure F.21: **Various plots for a MIS.** The three different column represents cuts [y-z], [x-z] and [y-x] respectively. The first row is the MIS for a cylinder ($n = 4$) and $d = 240\,\mathrm{nm}$ with no scattering, but the scatterer is shown as a thin outline. Second row shows the scattered part of the beam and the third row is the total beam.

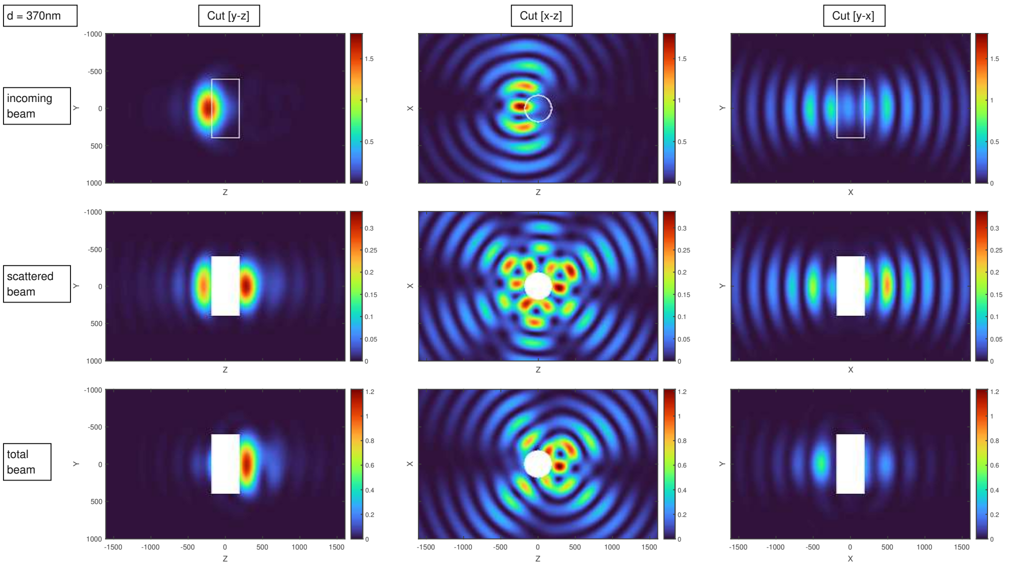

Figure F.22: **Various plots for a MIS.** The three different column represents cuts [y-z], [x-z] and [y-x] respectively. The first row is the MIS for a cylinder ($n = 4$) and $d = 370\,\text{nm}$ with no scattering, but the scatterer is shown as a thin outline. Second row shows the scattered part of the beam and the third row is the total beam.

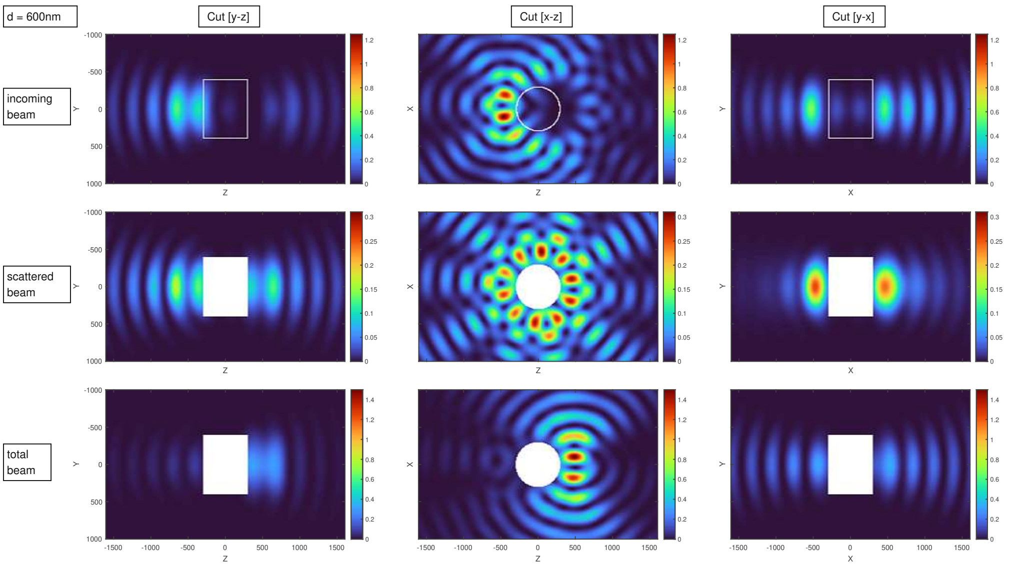

Figure F.23: **Various plots for a MIS.** The three different column represents cuts [y-z], [x-z] and [y-x] respectively. The first row is the MIS for a cylinder ($n = 4$) and $d = 600\,\text{nm}$ with no scattering, but the scatterer is shown as a thin outline. Second row shows the scattered part of the beam and the third row is the total beam.

List of Figures

List of Tables

Bibliography

[1] J. Ring and C. L. Stephens. “The Application of Michelson Interferometers to High Resolution Astronomical Spectrometry”. In: *Monthly Notices of the Royal Astronomical Society* 158.1 (June 1972), 5P–9P. ISSN: 0035-8711. DOI: 10.1093/mnras/158.1.5P.

[2] Daping Chu et al. “Digital Holography and 3D Imaging: introduction to the joint feature issue in Applied Optics and Journal of the Optical Society of America A”. In: *J. Opt. Soc. Am. A* 40.4 (Apr. 2023), DH1–DH3. DOI: 10.1364/JOSAA.490261.

[3] Yoshiyasu Ichikawa, Shunsuke Koike, and Kazuyuki Nakakita. “Measurement of a flow-velocity profile using a laser Doppler velocimetry coupled with a focus tunable lens”. In: *OSA Continuum* 3.7 (July 2020), pp. 1781–1791. DOI: 10.1364/OSAC.393866.

[4] Sylvain Gigan et al. “Roadmap on wavefront shaping and deep imaging in complex media”. In: *Journal of Physics: Photonics* 4.4 (Aug. 2022), p. 042501. DOI: 10.1088/2515-7647/ac76f9.

[5] Dorian Bouchet, Stefan Rotter, and Allard P. Mosk. “Maximum information states for coherent scattering measurements”. In: *Nature Physics* 17.5 (Jan. 2021), pp. 564–568. ISSN: 1745-2481. DOI: 10.1038/s41567-020-01137-4.

[6] Yoav Shechtman et al. “Optimal Point Spread Function Design for 3D Imaging”. In: *Phys. Rev. Lett.* 113 (13 Sept. 2014), p. 133902. DOI: 10.1103/PhysRevLett.113.133902.

[7] Tongjun Liu et al. “Picophotonic localization metrology beyond thermal fluctuations”. In: *Nature Materials* 22.7 (May 2023), pp. 844–847. ISSN: 1476-4660. DOI: 10.1038/s41563-023-01543-y.

[8] L. Lorenz. *Lysbevægelsen i og uden for en af plane Lysbølger belyst Kugle*. Kongelige Danske Videnskabernes Selskabs Skrifter: Naturvidenskabelig og Mathematisk Afdeling. 1890. URL: https://books.google.at/books?id=hnE7QwAACAAJ.

[9] Gustav Mie. “Beiträge zur Optik trüber Medien, speziell kolloidaler Metallösungen”. In: *Annalen der Physik* 330.3 (1908), pp. 377–445. DOI: https://doi.org/10.1002/andp.19083300302.

[10] P.C. Waterman. “Matrix formulation of electromagnetic scattering”. In: *Proceedings of the IEEE* 53.8 (1965), pp. 805–812. DOI: 10.1109/PROC.1965.4058.

[11] P. C. Waterman. "Symmetry, Unitarity, and Geometry in Electromagnetic Scattering". In: *Phys. Rev. D* 3 (4 Feb. 1971), pp. 825–839. DOI: 10.1103/PhysRevD.3.825.

[12] Timo A Nieminen et al. "Optical tweezers computational toolbox". In: *Journal of Optics A: Pure and Applied Optics* 9.8 (July 2007), S196. DOI: 10.1088/1464-4258/9/8/S12.

[13] Taylor Jonathan M. *Optical Binding Phenomena: Observations and Mechanisms.* Springer Science & Business Media, 2011.

[14] J Taylor and G Love. "Multipole expansion of Bessel and Gaussian beams for Mie scattering calculations". In: *Journal of the Optical Society of America. A, Optics, image science, and vision* 26 (Mar. 2009), pp. 278–82. DOI: 10.1364/JOSAA.26.000278.

[15] T.A Nieminen, H Rubinsztein-Dunlop, and N.R Heckenberg. "Multipole expansion of strongly focussed laser beams". In: *Journal of Quantitative Spectroscopy and Radiative Transfer* 79–80 (June 2003), pp. 1005–1017. ISSN: 0022-4073. DOI: 10.1016/s0022-4073(02)00335-7. URL: http://dx.doi.org/10.1016/S0022-4073(02)00335-7.

[16] Warren Wiscombe. "Improved Mie Scattering Algorithms". In: *Applied optics* 19 (May 1980), pp. 1505–9. DOI: 10.1364/AO.19.001505.

[17] T.A Nieminen, H Rubinsztein-Dunlop, and N.R Heckenberg. "Calculation of the T-matrix: general considerations and application of the point-matching method". In: *Journal of Quantitative Spectroscopy and Radiative Transfer* 79-80 (2003). Electromagnetic and Light Scattering by Non-Spherical Particles, pp. 1019–1029. ISSN: 0022-4073. DOI: https://doi.org/10.1016/S0022-4073(02)00336-9.

[18] Daniel W. Mackowski. "Discrete dipole moment method for calculation of the T matrix for nonspherical particles". In: *J. Opt. Soc. Am. A* 19.5 (May 2002), pp. 881–893. DOI: 10.1364/JOSAA.19.000881.

[19] W.R.C. Somerville, B. Auguié, and E.C. Le Ru. "smarties: User-friendly codes for fast and accurate calculations of light scattering by spheroids". In: *Journal of Quantitative Spectroscopy and Radiative Transfer* 174 (2016), pp. 39–55. ISSN: 0022-4073. DOI: https://doi.org/10.1016/j.jqsrt.2016.01.005.

[20] Philipp Ambichl et al. "Focusing inside Disordered Media with the Generalized Wigner-Smith Operator". In: *Phys. Rev. Lett.* 119 (3 July 2017), p. 033903. DOI: 10.1103/PhysRevLett.119.033903.

[21] G. Videen. "Light Scattering from a Sphere Near a Plane Interface". In: *Light Scattering from Microstructures.* Ed. by Fernando Moreno and Francisco González. Berlin, Heidelberg: Springer Berlin Heidelberg, 2000, pp. 81–96. ISBN: 978-3-540-46614-7.

[22] Nail A. Gumerov and Ramani Duraiswami. "Recursions for the Computation of Multipole Translation and Rotation Coefficients for the 3-D Helmholtz Equation". In: *SIAM Journal on Scientific Computing* 25.4 (2004), pp. 1344–1381. DOI: 10.1137/S1064827501399705.

[23] E. Wigner. *Gruppentheorie und ihre Anwendung auf die Quantenmechanik der Atomspektren*. Vieweg, 1977.

[24] R. A. Fisher and Edward John Russell. "On the mathematical foundations of theoretical statistics". In: *Philosophical Transactions of the Royal Society of London. Series A, Containing Papers of a Mathematical or Physical Character* 222.594-604 (1922), pp. 309–368. DOI: 10.1098/rsta.1922.0009.

[25] Mark J. Schervish. *Theory of Statistics*. New York: Springer, 1995. ISBN: 978-0-387-94546-0.

[26] Wikipedia contributors. *Fisher information — Wikipedia, The Free Encyclopedia*. [Online; accessed 10-January-2025]. 2024. URL: https://en.wikipedia.org/w/index.php?title=Fisher_information&oldid=1265029086.

[27] Dorian Bouchet et al. "Optimal Control of Coherent Light Scattering for Binary Decision Problems". In: *Phys. Rev. Lett.* 127 (25 Dec. 2021), p. 253902. DOI: 10.1103/PhysRevLett.127.253902.

[28] Richard A Waltz et al. "An interior algorithm for nonlinear optimization that combines line search and trust region steps". In: *Mathematical programming* 107.3 (2006), pp. 391–408.

[29] Richard H Byrd, Jean Charles Gilbert, and Jorge Nocedal. "A trust region method based on interior point techniques for nonlinear programming". In: *Mathematical programming* 89 (2000), pp. 149–185.

[30] BA Davey. *Introduction to Lattices and Order*. Cambridge University Press, 2002.

[31] Isaac C.D. Lenton et al. "OTSLM toolbox for Structured Light Methods". In: *Computer Physics Communications* 253 (Aug. 2020), p. 107199. ISSN: 0010-4655. DOI: 10.1016/j.cpc.2020.107199. URL: http://dx.doi.org/10.1016/j.cpc.2020.107199.

[32] Une Gabriele Butaite. "Enhanced optical tweezing: from hydrodynamic micromanipulation to optimised optical trapping". PhD thesis. University of Glasgow, 2020.

[33] Rodrigo Gutiérrez-Cuevas et al. "Reaching the precision limit with tensor-based wavefront shaping". In: *Nature Communications* 15.1 (2024), p. 6319.

[34] Manuel Nieto-Vesperinas. *2 - Fundamentals of Mie scattering*. Ed. by Igal Brener et al. Woodhead Publishing Series in Electronic and Optical Materials. Woodhead Publishing, 2020, pp. 39–72. ISBN: 978-0-08-102403-4. DOI: https://doi.org/10.1016/B978-0-08-102403-4.00007-4.

[35] Wikipedia contributors. *Mie scattering — Wikipedia, The Free Encyclopedia.* [Online; accessed 16-January-2025]. 2024. URL: https://en.wikipedia.org/w/index.php?title=Mie_scattering&oldid=1261739166.

[36] Manuel S. Stein, Amine Mezghani, and Josef A. Nossek. "A Lower Bound for the Fisher Information Measure". In: *CoRR* abs/1306.2607 (2013).

[37] MathWorks. *fmincon.* [Online; accessed 24-February-2025]. 2025. URL: https://www.mathworks.com/help/optim/ug/fmincon.html.